



HAL
open science

Species-selective targeting of pathogens revealed by the atypical structure and active site of *Trypanosoma cruzi* histone deacetylase DAC2

Martin Marek, Elizabeth Ramos-Morales, Gisele F A Picchi-Constante, Theresa Bayer, Carina Norström, Daniel Herp, Policarpo A Sales-Junior, Eloise P Guerra-Slompo, Kristin Hausmann, Alokta Chakrabarti, et al.

► To cite this version:

Martin Marek, Elizabeth Ramos-Morales, Gisele F A Picchi-Constante, Theresa Bayer, Carina Norström, et al.. Species-selective targeting of pathogens revealed by the atypical structure and active site of *Trypanosoma cruzi* histone deacetylase DAC2. *Cell Reports*, 2021, 37, 10.1016/j.celrep.2021.110129 . hal-03504175

HAL Id: hal-03504175

<https://hal.science/hal-03504175>

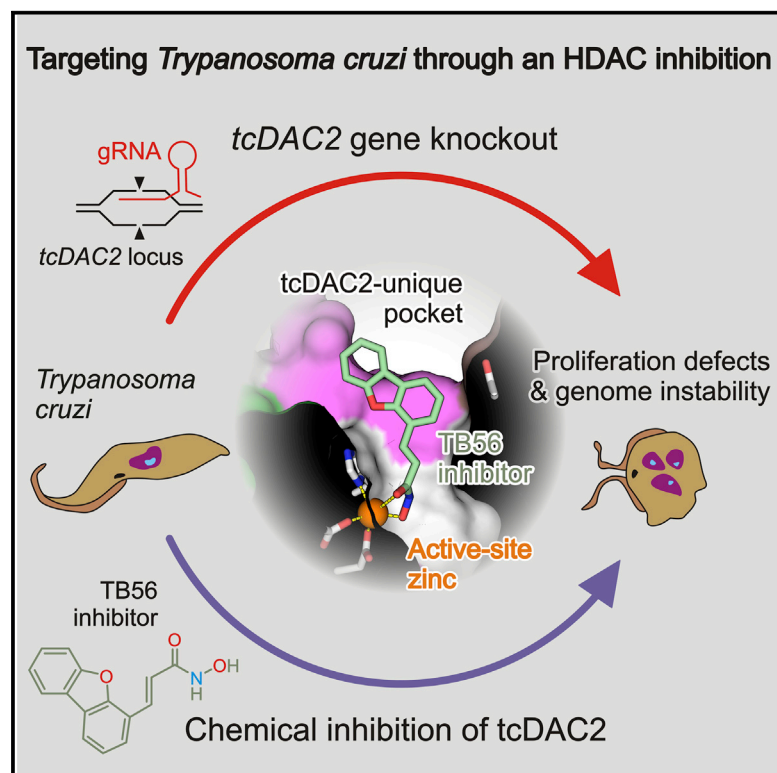
Submitted on 28 Dec 2021

HAL is a multi-disciplinary open access archive for the deposit and dissemination of scientific research documents, whether they are published or not. The documents may come from teaching and research institutions in France or abroad, or from public or private research centers.

L'archive ouverte pluridisciplinaire **HAL**, est destinée au dépôt et à la diffusion de documents scientifiques de niveau recherche, publiés ou non, émanant des établissements d'enseignement et de recherche français ou étrangers, des laboratoires publics ou privés.

Species-selective targeting of pathogens revealed by the atypical structure and active site of *Trypanosoma cruzi* histone deacetylase DAC2

Graphical abstract



Authors

Martin Marek, Elizabeth Ramos-Morales, Gisele F.A. Picchi-Constante, ..., Wolfgang Sippl, Nilson I.T. Zanchin, Christophe Romier

Correspondence

nilson.zanchin@fiocruz.br (N.I.T.Z.), romier@igbmc.fr (C.R.)

In brief

Marek et al. show that histone deacetylases (HDACs) from trypanosomes diverge from human HDACs. Notably, *T. cruzi* HDACs tcDAC1 and tcDAC2 are essential. tcDAC2 has structural features unobserved in human HDACs that promote specific interactions with inhibitors. Thus, targeting atypical HDACs from pathogens can lead to anti-parasitic strategies.

Highlights

- Trypanosome histone deacetylases (HDACs) significantly diverge from human HDACs
- *T. cruzi* class I HDACs tcDAC1 and tcDAC2 are essential to the parasite viability
- tcDAC2 deacetylase activity can be inhibited by targeting its atypical active site
- *T. cruzi* parasites can be targeted through a tcDAC2-specific inhibitor



Article

Species-selective targeting of pathogens revealed by the atypical structure and active site of *Trypanosoma cruzi* histone deacetylase DAC2

Martin Marek,^{1,2,9,10} Elizabeth Ramos-Morales,^{1,2,9} Gisele F.A. Picchi-Constante,^{3,9} Theresa Bayer,⁴ Carina Norström,⁵ Daniel Herp,⁶ Policarpo A. Sales-Junior,⁷ Eloise P. Guerra-Slompo,³ Kristin Hausmann,⁴ Alokta Chakrabarti,⁶ Tajith B. Shaik,^{1,2} Annika Merz,⁶ Edouard Troesch,^{1,2} Karin Schmidtkunz,⁶ Samuel Goldenberg,³ Raymond J. Pierce,⁸ Marina M. Mourão,⁷ Manfred Jung,⁶ Johan Schultz,⁵ Wolfgang Sippl,⁴ Nilson I.T. Zanchin,^{3,*} and Christophe Romier^{1,2,11,*}

¹Université de Strasbourg, CNRS, INSERM, Institut de Génétique et de Biologie Moléculaire et Cellulaire, UMR 7104, U 1258, 67404 Illkirch, France

²IGBMC, Department of Integrated Structural Biology, 1 rue Laurent Fries, B.P. 10142, 67404 Illkirch Cedex, France

³Instituto Carlos Chagas, Fiocruz Paraná, Curitiba, Paraná 81350-010, Brazil

⁴Institute of Pharmacy, Martin-Luther-Universität Halle-Wittenberg, Wolfgang-Langenbeck-Straße 4, 06120 Halle/Saale, Germany

⁵Kancera AB, Nanna Svartz Väg 4, SE-17165 Solna, Sweden

⁶Institute of Pharmaceutical Sciences, Albert-Ludwigs-Universität Freiburg, Albertstraße 25, 79104 Freiburg, Germany

⁷Instituto René Rachou, Fundação Oswaldo Cruz, Avenida Augusto de Lima, 1715, 30190-002 Belo Horizonte, Brazil

⁸Univ. Lille, CNRS, Inserm, CHU Lille, Institut Pasteur de Lille, U1019 - UMR 9017 - CIL - Centre d'Infection et d'Immunité de Lille, 59000 Lille, France

⁹These authors contributed equally

¹⁰Present address: Loschmidt Laboratories, Department of Experimental Biology & RECETOX, Faculty of Science, Masaryk University, Kamenice 5/C13, 625 00 Brno, Czech Republic

¹¹Lead contact

*Correspondence: nilson.zanchin@fiocruz.br (N.I.T.Z.), romier@igbmc.fr (C.R.)

<https://doi.org/10.1016/j.celrep.2021.110129>

SUMMARY

Writing and erasing of posttranslational modifications are crucial to phenotypic plasticity and antigenic variation of eukaryotic pathogens. Targeting pathogens' modification machineries, thus, represents a valid approach to fighting parasitic diseases. However, identification of parasitic targets and the development of selective anti-parasitic drugs still represent major bottlenecks. Here, we show that the zinc-dependent histone deacetylases (HDACs) of the protozoan parasite *Trypanosoma cruzi* are key regulators that have significantly diverged from their human counterparts. Depletion of *T. cruzi* class I HDACs tcDAC1 and tcDAC2 compromises cell-cycle progression and division, leading to cell death. Notably, tcDAC2 displays a deacetylase activity essential to the parasite and shows major structural differences with human HDACs. Specifically, tcDAC2 harbors a modular active site with a unique subpocket targeted by inhibitors showing substantial anti-parasitic effects *in cellulo* and *in vivo*. Thus, the targeting of the many atypical HDACs in pathogens can enable anti-parasitic selective chemical impairment.

INTRODUCTION

High phenotypic plasticity and antigenic variation is a hallmark of eukaryotic parasites, enabling them to adapt to different hosts and escape their immune surveillance. Cumulative evidence shows that the processes regulating the writing, reading, and erasing of protein posttranslational modifications (e.g., phosphorylation, acetylation, methylation) in many cellular actors play a prominent role in these transformations, notably through epigenetic modifications. Effectors in these regulatory pathways in pathogens, thus, represent important potential drug targets, and repurposing of drugs targeting them has been identified as an effective strategy to reduce the time and financial costs associated with anti-parasitic drug development (Andrews et al.,

2012a, 2012b, 2014; Wang et al., 2015; Hailu et al., 2017; Schiedel and Conway, 2018; Fioravanti et al., 2020). Combining repurposing with a piggyback strategy, where the chemical scaffolds of the repurposed drugs are modified, can further foster the design of parasite-selective compounds with little or no cross-reactivity with human enzymes.

Currently, most approved epigenetic drugs target zinc-dependent histone lysine deacetylases (HDACs) (Eckschlager et al., 2017; Falkenberg and Johnstone, 2014; Li and Seto, 2016). This explains why repurposing of HDAC inhibitors to fight neglected diseases is receiving considerable attention (Andrews et al., 2012a, 2012b, 2014; Wang et al., 2015; Hailu et al., 2017; Fioravanti et al., 2020). Acetylation of lysines in eukaryotes is a major reversible posttranslational modification that links



metabolism to cell signaling and plays a critical role in the regulation of key cellular processes (Choudhary et al., 2009, 2014; Drazic et al., 2016; Marmorstein and Zhou, 2014; Seto and Yoshida, 2014; Verdin and Ott, 2015; Narita et al., 2019). In humans, the dysregulation of acetylation mechanisms is implicated in the onset and progression of numerous diseases (Eckschlager et al., 2017; Falkenberg and Johnstone, 2014; Fujisawa and Filippakopoulos, 2017; Li and Seto, 2016). Nevertheless, the reversible nature of acetylation can be used to pharmacologically modulate eukaryotic acetylation pathways (Eckschlager et al., 2017; Falkenberg and Johnstone, 2014; Li and Seto, 2016; Schiedel and Conway, 2018).

HDACs are named according to their similarity with the 11 human HDAC isozymes, which have been divided into four classes: class I (HDAC1, 2, 3, 8), class IIa (HDAC4, 5, 7, 9), class IIb (HDAC6, 10), and class IV (HDAC11) (Porter and Christianson, 2019; Seto and Yoshida, 2014). Specifically, class IIa HDACs have lost their essential catalytic tyrosine, replaced by a histidine, and are thought to play a scaffolding role in macromolecular complexes (Desravines et al., 2017; Hudson et al., 2015; Park et al., 2018). Not only histones, but also other non-histone proteins, are targeted by the various active HDAC isozymes, which can even display specific or dual deacetylation and deacetylation activities (Sabari et al., 2017; Narita et al., 2019).

We have previously used repurposing and piggyback strategies, combining structure-based and high-throughput screening approaches on smHDAC8, the homolog of human class I HDAC8 from the parasitic flatworm *Schistosoma mansoni* that causes schistosomiasis. Our studies have led to the design of smHDAC8-selective inhibitors but have also enabled the characterization of the structure/function relationships of HDAC8 enzymes to help with the development of selective anti-cancer drugs (Bayer et al., 2018; Heimbürg et al., 2016, 2017; Marek et al., 2013, 2015, 2018). This work has highlighted the challenge in developing selective anti-parasitic drugs targeting HDACs, notably due to the high structural similarity of the active sites of smHDAC8 and human HDACs. However, HDACs from other parasites show stronger phylogenetic differences with human HDAC enzymes, suggesting that the selectivity issue might be easier to overcome in these parasites (Scholte et al., 2017; Wang et al., 2015).

This is the case of the HDACs of *Trypanosoma brucei* and *Trypanosoma cruzi* that are responsible for African trypanosomiasis (sleeping sickness; Büscher et al., 2017) and American trypanosomiasis (Chagas disease; Pérez-Molina and Molina, 2018), respectively. While the fight against human African trypanosomiasis has made significant progress, with only a few tens of thousands of people infected and a continuous decrease in new cases each year, Chagas disease remains a major threat, with millions of people infected and tens of thousands of yearly deaths (Büscher et al., 2017; Pérez-Molina and Molina, 2018; Varikuti et al., 2018). Notably, the side effects and the acute phase-restricted efficacy of the drugs Benznidazole (BZN) and Nifurtimox, currently used to treat Chagas disease, are major issues and call for the development of new drugs (Scarim et al., 2018; Varikuti et al., 2018).

Four HDACs are found in *T. cruzi* and *T. brucei* that show restricted phylogenetic resemblance to human HDACs and

that have been attributed to HDAC class I (tcDAC1/tbDAC1 and tcDAC2/tbDAC2) and class IIb (tcDAC3/tbDAC3 and tcDAC4/tbDAC4) (Scholte et al., 2017). So far, functional characterization of these HDACs has predominantly been performed in *T. brucei*, showing that tbDAC1 and tbDAC3, but not tbDAC2 and tbDAC4, are essential and act in helping the parasite to evade the host immune response (Ingram and Horn, 2002; Wang et al., 2010). In contrast, little is known about *T. cruzi* HDACs. Importantly, protein acetylation patterns in both pathogenic species are different, even for histone proteins, suggesting substantial functional divergences in the acetylation pathways of these flagellate parasites (Mandava et al., 2007; Moretti et al., 2018; Picchi et al., 2017).

Treatments of both *T. brucei* and *T. cruzi* parasites with HDAC inhibitors have identified molecules that could potentially target these protozoans, but direct repurposing was impaired due to toxicity problems. However, these studies suggested the presence of unique features within the trypanosome HDACs that could be exploited to develop selective inhibitors targeting these enzymes (Andrews et al., 2012a; Campo, 2017; Carrillo et al., 2015; Engel et al., 2015; Hailu et al., 2017; Kelly et al., 2012; Scarim et al., 2018; Varikuti et al., 2018; Zuma and de Souza, 2018; Fioravanti et al., 2020).

Here, we show that trypanosome HDACs harbor very specific features compared to human HDACs. Surprisingly, *T. cruzi* class I HDACs tcDAC1 and tcDAC2 are both functionally essential to the parasite, in contrast to *T. brucei*, where only tbDAC1 is essential. Specifically, tcDAC2 has retained canonical functional determinants and displays an acetyl-lysine deacetylase activity that can be inhibited. The crystal structures of tcDAC2, bound to different inhibitors, reveal a zinc-dependent deacetylase fold, but with major differences in its overall structure as well as in its active site compared to the various human HDACs. Notably, the loops forming the tcDAC2 active site show structural similarities either with loops of the HDAC1/HDAC2/HDAC3 (hereafter termed HDAC1-3) isozyme family or with loops of the HDAC8 isozyme, revealing the combinatorial modularity of HDAC active sites. Importantly, tcDAC2 harbors a unique pocket in its active site that is targeted by one of the inhibitors used in our study. *In cellulo* and *in vivo*, parasitic infection is affected by this inhibitor, which, thus, represents a starting scaffold for designing more potent and more selective inhibitors targeting tcDAC2. Collectively, our results reveal the atypical nature of the *Trypanosoma cruzi* DAC2 lysine deacetylase, which extends to other parasitic HDACs and paves the way to the rational design of selective inhibitors to fight Chagas and, potentially, other parasitic diseases.

RESULTS

Trypanosome HDACs are atypical

Phylogenetic analyses have suggested that DAC1 enzymes are more related to the HDAC1-3 isozyme family, but DAC2, DAC3, and DAC4 enzymes could not be assigned to a specific isozyme family (Ingram and Horn, 2002; Scholte et al., 2017). We have extended sequence analyses to better understand the divergences observed. Specifically, two contiguous residues at the tip of HDAC active site L6 loop inform on HDAC isozyme

family, partners, and substrates (Millard et al., 2013; Watson et al., 2012, 2016; Hai and Christianson, 2016; Miyake et al., 2016; Hai et al., 2017; Porter and Christianson, 2019; Marek et al., 2018). In DAC1 enzymes, an arginine-leucine (RL) motif is found (Figure S1A), which is typical of HDAC1-3 isozymes, where the arginine plays an essential role for recruiting partners and for activity (Millard et al., 2013; Watson et al., 2012, 2016).

In contrast, in DAC2 a proline-leucine (PL; tcDAC2) or proline-tyrosine (PY; tbDAC2) motif is found, reminiscent of both class I HDAC8 proline-methionine (PM) and class II PL motifs (Figures 1 and S1B). Surprisingly, in DAC3, a leucine-leucine (LL) motif is found, which is not observed in any other trypanosome or human HDACs (Figure S2A), while DAC4 displays a canonical class II PL motif (Figure S2B). Additional sequence analyses (Figure S2) further show that DAC3 and DAC4 have a single catalytic domain, in contrast to the tandem domains observed in human class IIb HDACs. Compared to human HDACs, DAC2, DAC3, and DAC4 also contain small-to-medium-size insertions in their catalytic domains whose roles are unknown. In addition, the catalytic domain of the DAC3 enzymes is split in its middle by a ~170-residue-long insertion that should protrude from the HDAC core without affecting its structural integrity (Figure S2A).

Further analyses of sequence identities/similarities between the catalytic domains of trypanosome and human HDACs show that all trypanosome HDACs have low identities (<40%) compared to human HDACs, with DAC2 and DAC4 showing the strongest divergence (identities <30%) (Figures S3A and S3B). Surprisingly, the identities/similarities are even lower when comparing the four parasitic isozymes among themselves, suggesting a strong functional divergence for each parasitic isozyme (Figure S3C). Moreover, comparisons of the same isozymes from *T. brucei* and *T. cruzi* also reveal considerable divergence (Figure S3C). While the DAC1 enzymes are strongly conserved (85% identity), DAC3 and DAC4 show intermediate conservation (64%), and the DAC2 enzymes have the lowest sequence identity (51%). These differences possibly relate to the changes in acetylation patterns observed in these two parasites (Mandava et al., 2007; Moretti et al., 2018; Picchi et al., 2017).

Strikingly, careful comparison of tbDAC2 and tcDAC2 sequences reveals major differences in their respective active sites. *T. brucei* DAC2, which has been shown to be non-essential (Ingram and Horn, 2002), has many active site residues involved in zinc coordination, acetyl-lysine binding, and catalysis replaced by non-canonical amino acids; this includes the replacement of its catalytic tyrosine by an asparagine, thus questioning its function as a bona fide deacetylase. In contrast, *T. cruzi* DAC2 has retained all canonical active site residues and could, therefore, have a fully functional deacetylase activity (Figures 1 and S1B). These sequence analyses confirm the atypical character of trypanosome HDACs, suggesting that they represent potential drug targets. Our results also highlight the unexpected difference between *T. brucei* and *T. cruzi* class I DAC2 enzymes, which

prompted us to further characterize trypanosome class I HDACs, notably tcDAC2.

***T. cruzi* DAC1 and DAC2 are both essential to the parasite**

We first investigated *in vivo* the essential character of *T. cruzi* class I HDACs. Gene-targeted deletion experiments by homologous recombination showed that both tcDAC1 and tcDAC2 are essential to *T. cruzi* since null parasites did not grow in culture and ended up dying over time. In addition, single- and double-allele knocked-out cells presented a lower proliferative rate than did wild-type (WT) parasites (Figures 2A and 2B), and DNA content quantification by flow cytometry revealed aberrant cell-cycle progression (Figures 2C and 2D) that could be explained by the presence of several abnormal cells containing multiple nuclei/kinetoplasts (Figure 2E).

To further investigate the unexpected essential character of tcDAC2 compared to tbDAC2, we complemented these results by generating null mutants with the CRISPR/Cas9 technology for *tcDAC2* using three different sgRNAs to direct Cas9 to distinct positions in the *tcDAC2* gene sequence. This strategy resulted in aberrant cells that were not able to divide, consistent with the phenotype expected for an essential gene. DNA content quantification by flow cytometry revealed abnormal cell-cycle progression (Figure 2F), with defects ranging from cells without DNA to cells with several nuclei/kinetoplasts (Figure 2G).

We then used the essential character of tcDAC2 to further characterize this enzyme by complementation assays with different constructions and by using a *T. cruzi* cell line stably expressing Cas9. An initial construction with the original *tcDAC2* DNA sequence in the sgRNA target region and encoding WT tcDAC2 (tcDAC2_sens) was used as a negative control. After sgRNA transfection, the cells transfected with the tcDAC2_sens construct showed abnormal cell-cycle and cell morphology along with reduced cell proliferation (Figures 2H, 2I, and S4). In contrast, cells transfected with a construction of WT tcDAC2 but containing an altered sequence not recognized by the sgRNA (tcDAC2_res) restored the WT phenotype (Figures 2H, 2I, and S4), confirming that the depletion of tcDAC2 causes lethality.

HDACs where the catalytic tyrosine is replaced by a phenylalanine are known to be mostly inactive. We used the same complementation strategy with a catalytic Y371F mutant of tcDAC2 whose DNA sequence was not recognized by the sgRNA (tcDAC2_Y371F). Our results showed that the cells containing the tcDAC2_Y371F construct presented a deleterious phenotype, similar to tcDAC2 knocked-out cells, as observed by alteration in cell-cycle progression, cell proliferation, and cell morphology (Figures 2H, 2I, and S4), showing the importance of tyrosine 371 for tcDAC2 function.

We then used the same strategy to investigate the long and highly acidic tcDAC2 C-terminal tail (Figure 1), whose functional role is unknown. The complementation strategy using a

residue gatekeeping the HDAC active sites. The green diamond marks the arginine that caps the tcDAC2 L6 loop. Purple circles mark important residues forming the tcDAC2-unique pocket. Secondary structure elements (α , α helices; β , β strands; η , 3_{10} -helices) from tcDAC2 are shown above the alignment. Sequence insertions in tcDAC2 are boxed (orange), and the three largest ones are labeled (insertions 1–3) below the alignment. The region removed for crystallization is shown in gray italics. Loops forming the active site are indicated and labeled in blue under the alignment.

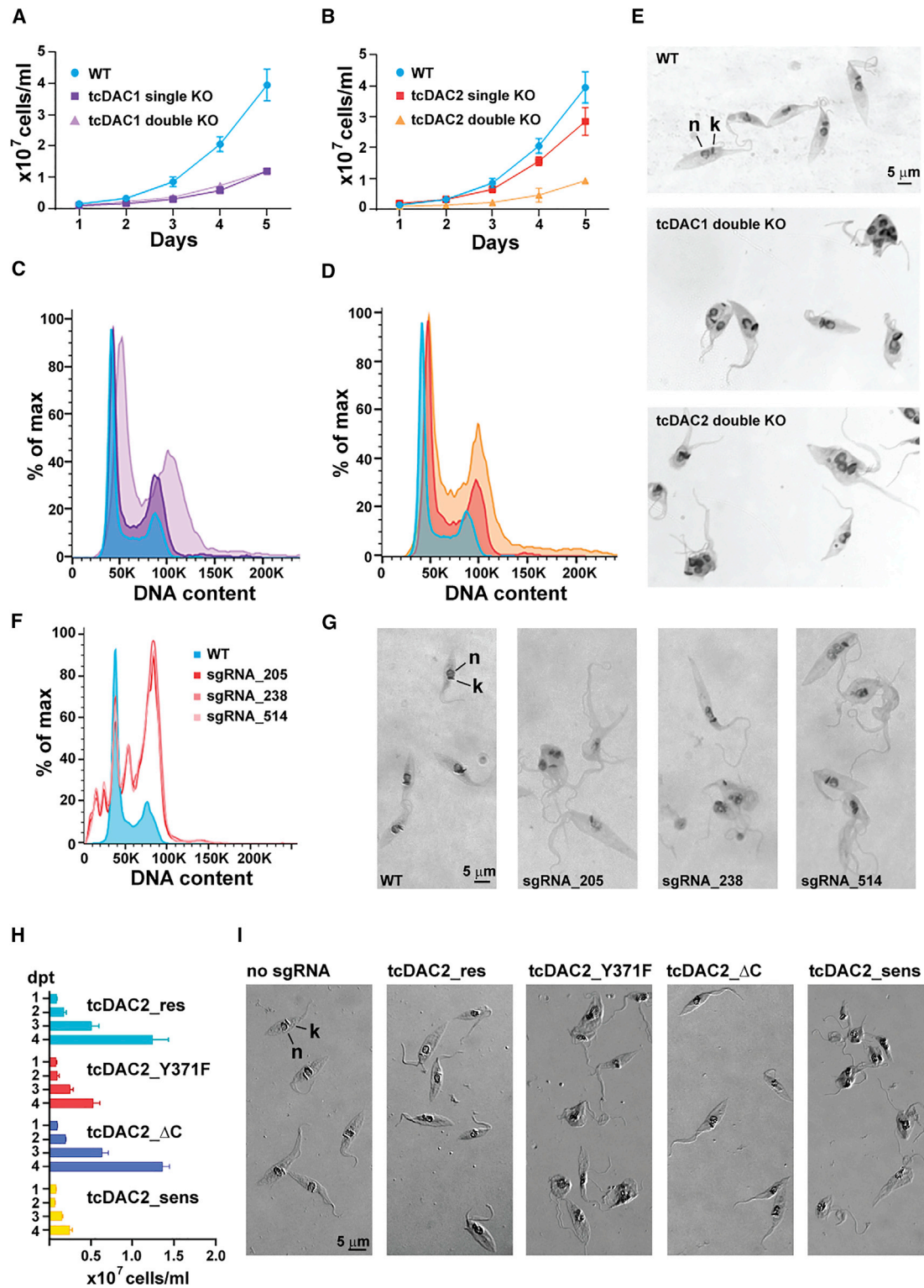


Figure 2. Lack of class I HDACs impacts cell cycle and proliferation of *T. cruzi*

(A and B) Growth curves showing that tcDAC1 and tcDAC2 knocked-out cells (purple and orange curves, respectively) present lower proliferation rates when compared to WT cells (light blue).

(C and D) Cell-cycle analyses show abnormal progression as determined by DNA content quantification. Blue, WT cells; dark and light purple, single and double tcDAC1 knocked-out cells; red and orange, single and double tcDAC2 knocked-out cells.

(legend continued on next page)

construction deleted for this C-terminal tail (tcDAC2_ΔC) showed that in contrast to the tcDAC2_Y371F mutant, cells expressing the tcDAC2_ΔC mutant did not present any detectable phenotype, showing that this tail is functionally dispensable *in vivo* (Figures 2H, 2I, and S4).

T. cruzi DAC2 possesses an acetyl-lysine deacetylase activity that can be inhibited

We next characterized tcDAC2 biochemically and biophysically using the shorter C-terminal construct of tcDAC2 (tcDAC2_ΔC), which is sufficient for parasitic survival and shows much higher solubility than the WT enzyme. Size-exclusion chromatography and dynamic light scattering analyses showed that tcDAC2_ΔC is mostly monomeric, suggesting tcDAC2 similarity with HDAC8. However, thermal shift assays revealed its lower thermal stability compared to human and *S. mansoni* HDAC8 enzymes (Figure 3A).

Deacetylation assays showed that tcDAC2_ΔC possesses an acetyl-lysine deacetylase activity, slightly lower than human HDAC8 on the substrates used (Figure 3B). In agreement with our *in vivo* experiments, the Y371F mutant was inactive (Figure 3B), suggesting that tcDAC2 has a bona fide deacetylase activity relying on its canonical catalytic residues. Inhibition assays were then performed using pan-HDAC (SAHA [Vorinostat], Quisnostat [QSN]), HDAC1-3-selective (Entinostat, Mocetinostat), and HDAC8-selective (PCI-34051, NCC-149) inhibitors as well as a set of in-house available HDAC inhibitors (TB51, TB56, TB72, and TB75) that we developed during the work on smHDAC8. We identified these latter compounds as putative tcDAC2 inhibitors by *in silico* docking experiments with a tcDAC2 model established using human and *S. mansoni* HDAC8 as templates. QSN and the TB compounds had IC₅₀ values in the low nM and μM range, respectively, showing that tcDAC2 deacetylase activity can be inhibited potently (Figure 3C; Table S1). However, neither SAHA nor any of the HDAC1-3-selective and HDAC8-selective inhibitors showed strong inhibitory effects in these assays.

T. cruzi DAC2 stabilization and structure determination

Attempts to crystallize the tcDAC2_ΔC protein yielded only unreplicable, poorly diffracting crystals. Since tcDAC2 contains several medium-sized insertions compared to human HDAC8 that could hamper crystallization (insertions 1, 2 and 3; Figure 1), we removed specific regions in these insertions to stabilize the enzyme and facilitate its crystallization. Our experiments on tcDAC2_ΔC showed that only partial deletions in insertion 2 can be tolerated in terms of solubility. Specifically, one precise deletion in this insertion led to a construct (tcDAC2_ΔIns2; Figure 1) showing significant increase in thermal (~10°C) and pro-

teolytic stability compared to tcDAC2_ΔC (Figures 3A and S5A), suggesting that the part removed is a solvent-exposed, possibly unstructured loop. The tcDAC2_ΔIns2 construct showed a moderately increased DAC activity compared to tcDAC2_ΔC (Figure 3B).

Importantly, the tcDAC2_ΔIns2 mutant could rescue the death phenotype of the tcDAC2 knockout *in vivo*, indicating that the part removed is not functionally essential for parasite survival (Figure S5B). The tcDAC2_ΔIns2 protein could be reproducibly crystallized, but the small crystals obtained did not diffract. Therefore, we looked at inhibitor-induced tcDAC2_ΔIns2 thermal stabilization using the most potent inhibitors characterized in our *in vitro* inhibition study. All inhibitors tested increased the thermal stability of the enzyme (Figure S5C). The highest increase was observed with the pan-HDAC inhibitor QSN (~18°C), followed by the inhibitors TB56 and TB75 (~13°C). Co-crystallization experiments with all tested inhibitors yielded crystals only in the presence of QSN and TB56.

The crystals of both complexes showed good diffraction, and complete crystallographic datasets could be collected at 1.75 Å (QSN) and 2.3 Å (TB56) resolution. Structure determination was performed by molecular replacement using our initial homology model of tcDAC2, and both tcDAC2/QSN and tcDAC2/TB56 structures were refined through manual building and automated refinement (Table S2).

T. cruzi DAC2 has an atypical class I HDAC structure

Our structures showed that tcDAC2_ΔIns2 (hereafter termed tcDAC2 for simplicity) possesses a classical arginase/HDAC fold composed of a central β sheet sandwiched between several α helices (Figure 4A). A search with DALI (Holm, 2020) showed unambiguous similarity of tcDAC2 with class I HDACs, notably HDAC8. Precise comparison revealed, however, that although a large N-terminal part of tcDAC2 superposes well with human class I HDACs, the majority of the C-terminal part of tcDAC2 turns out to be structurally divergent (Figure 4B). This was surprising since all human class I enzymes (HDAC1-3 and HDAC8) show a high similarity in their overall structures, with differences being mostly observed at the amino acid level and for the conformation of some active site loops (Figure 4B).

The differences observed between tcDAC2 and class I human HDACs start from the end of tcDAC2 α8-helix, which is longer than its human counterparts. Following this helix, insertion 3 is fully visible in our two tcDAC2 structures and packs tightly against the tcDAC2 core, forming specific interactions (Figure 4B). Interestingly, many of the aforementioned small-sequence insertions found in tcDAC2, compared to human HDAC1-3 and HDAC8 (Figures 1 and S1B), appear to form small

(E) Light microscopy images showing an increase in the number of nuclei/kinetoplasts in tcDAC1 and tcDAC2 knocked-out cells.

(F) Abnormal cell-cycle progression observed for all three different sgRNAs used in tcDAC2 disruption using the CRISPR-Cas9 methodology. Cyan blue curve, WT cells; red line curves, null mutant cells.

(G) Light microscopy images showing an increase in the number of nuclei/kinetoplasts in tcDAC2 knocked-out cells using the CRISPR-Cas9 methodology.

(H and I) Cell proliferation rates (H) and light microscopy images (I) of parasites from tcDAC2 complementation assays. tcDAC2_sens, negative control (knockout phenotype); tcDAC2_res, positive control; tcDAC2_Y371F, substitution of the catalytic tyrosine residue by a phenylalanine; tcDAC2_ΔC, deletion of the glutamic acid-rich C-terminal region. n, nucleus; k, kinetoplast; dpt, days post-transfection.

Assays reported were done as biological duplicates (A and B) and technical triplicates (H). In (A), (B), and (H), data are represented as mean ± SD. Cell-cycle analyses shown in (C), (D), and (F) represent data from at least 10,000 single cells. In (E), (G), and (I), scale bars represent 5 μM.

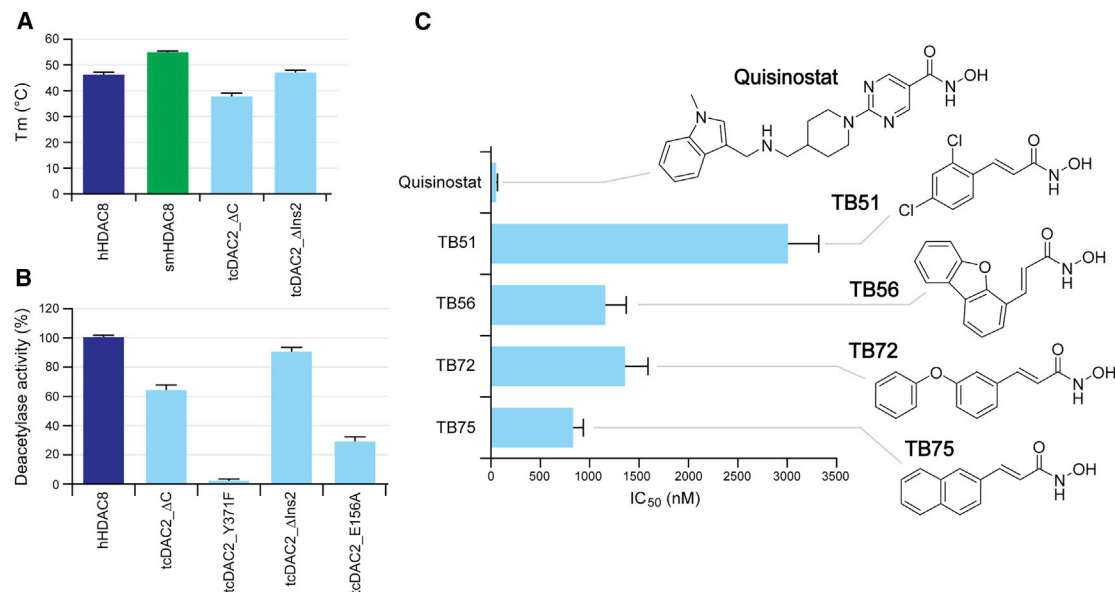


Figure 3. tcDAC2 is a functional acetyl-lysine deacetylase that is inhibited by drug-like inhibitors

(A) Thermal stability (°C) of human (h) HDAC8 (dark blue), *Schistosoma mansoni* (sm) HDAC8 (green), and the *Trypanosoma cruzi* (tc) DAC2_ΔC and DAC2_ΔIns2 constructs (cyan). The thermal stability of tcDAC2 is lower than that of HDAC8 enzymes but can be increased by removing a small region of insertion 2. (B) Measurements of the deacetylase activity of hHDAC8 and various tcDAC2 constructs. The deacetylase activity is increased upon removal of the small region of insertion 2 that stabilizes the enzyme but is decreased by the mutation of important active site residues. (C) Structures and IC₅₀ values for tcDAC2 of various inhibitors. Detailed IC₅₀ values, including for other human HDACs, are provided in Table S1. All assays done in triplicate. All data are represented as mean ± SD.

extended loops in the vicinity of insertion 3, defining a specific surface on tcDAC2. Similarly, insertion 1, which is only partially seen in the density in our structures, is also found in the vicinity of insertion 3, packing against the tcDAC2 core and also participating in this tcDAC2-specific surface (Figure 4B).

Following insertion 3, the only structurally similar part between the tcDAC2 C-terminal region and the same region in human HDAC1-3 and HDAC8 concerns the region spanning the 3₁₀-helix η10 that adopts a common fold and is similarly positioned in all these enzymes (Figures 1 and 4B). However, tcDAC2, again, diverges structurally from human class I HDACs immediately after this region. Specifically, whereas human class I HDACs have a short, straight stretch of residues (LC loop) that links the η10 region to their αC-helix, the tcDAC2 LC loop harbors additional residues that form a bulge extending toward the active site. This tcDAC2 extended LC loop lies over the active site L6 loop, with the side chain of arginine R439 forming a bidentate interaction with L6 loop main chain carbonyls (Figure 4C).

This longer LC loop of tcDAC2 ends at the same position where human HDAC αC-helices start, with these latter human helices packing tightly against their HDAC cores through multiple hydrophobic interactions. Surprisingly, an αC-helix in tcDAC2 is observed only for the tcDAC2/TB56 complex and not for the tcDAC2/QSN complex, where no electron density is observed. In addition, the tcDAC2 αC-helix does not pack against the HDAC core but, instead, projects away from this core and is involved in crystal packing (Figure S6A).

We have tentatively modeled the binding of the tcDAC2 αC-helix as observed in human HDAC1 and HDAC8. An interaction

similar to that observed in the human HDACs appears impossible in tcDAC2, with both surfaces displaying a positive charge (Figure S6A). In fact, as seen in our two tcDAC2 structures, a few residues preceding and starting the tcDAC2 αC-helix form specific hydrophobic interactions with the tcDAC2 core and position the start of the tcDAC2 αC-helix differently (Figure S6B). The fact that this helix is not observed in the tcDAC2/QSN structure—although our two structures otherwise superpose very well—suggests that this region is disordered and could fold only upon interaction with a partner and/or a substrate.

Finally, we have shown that part of tcDAC2 insertion 2 could be removed for crystallization. While the remaining part of insertion 2 mostly interacts with the tcDAC2 core, our structures show that the region removed for crystallization would most likely bulge out of the structure without making strong contact with the rest of the protein (Figure 4A). Interestingly, superposition of tcDAC2 with the hSHDAC1/MTA1 (PDB code 4bkx) and hSHDAC3/NCOR (PDB code 4a69) complexes shows that insertion 2, but also insertion 1, would clash with the binding of either MTA1 or NCOR homologs (Figure 4D). This latter feature, in addition to the absence of an arginine in the tcDAC2 L6 loop and the observed monomeric form of this enzyme, further supports the functional difference between tcDAC2 and the isoforms of the HDAC1-3 family.

T. cruzi DAC2 active site displays HDAC1-3 and HDAC8 features

As expected from our sequence analyses, tcDAC2 has a zinc ion at the bottom of its active site, which is coordinated canonically

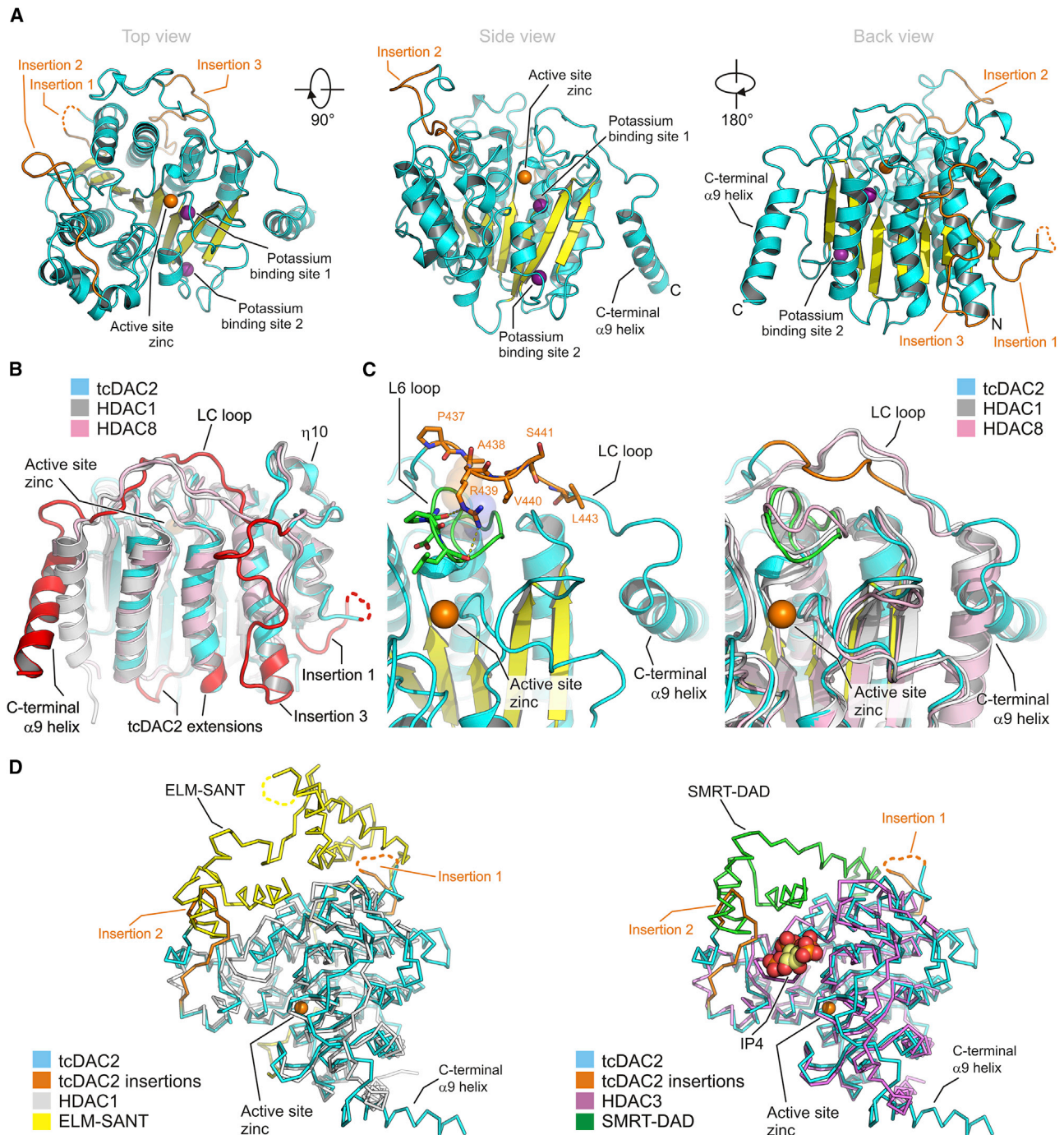


Figure 4. Atypical structure of tcDAC2

(A) Ribbon representation of the tcDAC2 structure in different views as observed in the tcDAC2/TB56 complex. The zinc (orange) and potassium (purple) ions are shown as spheres, helices are colored cyan, and β strands are colored yellow. The largest insertions found in tcDAC2 compared to human HDACs are shown in orange. The C-terminal α 9 helix of tcDAC2, which binds in a non-canonical position, is labeled.

(B) Ribbon representation of the tcDAC2-specific surface. Regions that diverge strongly at the sequence and structural level from the canonical sequences and folds observed in human class I HDACs are colored red, revealing that they mostly concentrate on a single side of the enzyme.

(C) Close-up view of tcDAC2 LC loop (orange) that caps the tcDAC2 active site L6 loop (green). Notably, LC loop arginine 439 interacts with L6 loop main chain carboxyl oxygens, firmly maintaining its capping position.

(D) Positioning of tcDAC2 insertions 1 and 2 that would interfere with partners binding as observed for human class I HDAC1 and HDAC3.

by the two aspartates (D237 and D328) and one histidine (H239) (hsHDAC8 D178, D267, and H180). Similarly, the catalytic tyrosine Y371 (hsHDAC8 Y306) is perfectly positioned to play a role in catalysis, as well as the histidine dyad H197 and H198 (hsHDAC8 H142 and H143) (Figure 5A). In addition, phenylalanines F207 and F267 (hsHDAC8 F152 and F208) form the hydrophobic tunnel that normally accommodates the aliphatic part of the incoming acetylated lysine. Finally, glutamate E156 is present at the position where hsHDAC8 D101 is positioned to interact with the main chain of the incoming acetylated lysine substrate (Figure 5A). Mutation of this glutamate to alanine (E156A) causes the reduction by half of tcDAC2 DAC activity (Figure 3B). Thus, tcDAC2 has a bona fide DAC active site also observed in other human class I enzymes (Figure 5A).

We next looked at the conformations of the loops forming the tcDAC2 active site and compared them to those of active site loops from human class I HDACs. Similar to what is observed among the different human HDACs, the loops forming the bottom of the tcDAC2 active site (L3, L4, and L7 loops) show no strong conformational changes compared to their human counterparts. Looking at the loops forming the upper part of the tcDAC2 active site pocket, we observe that the tcDAC2 L1 loop is very similar to the hsHDAC8 L1 loop; this loop is much shorter than that of the hsHDAC1-3 isozyme family (Figure 5B). Likewise, a strong structural similarity is observed between tcDAC2 and hsHDAC8 L2 and L5 loops, while those of hsHDAC1-3 adopt a slightly different conformation (Figure 5B).

Surprisingly, however, this is not the case for the tcDAC2 L6 loop that adopts a bona fide hsHDAC1-3 L6 loop conformation, markedly different from that of the hsHDAC8 L6 loop (Figure 5B). A conformational change of this loop in tcDAC2 appears highly unlikely since it is covered and appears kept in position by the LC loop of tcDAC2, notably R439 (Figure 4C). This agrees with our previous observation of the high conformational stability of the hsHDAC8 L6 loop despite its full replacement by that of hsHDAC1 (Marek et al., 2018).

T. cruzi DAC2 contains a unique active site pocket that can be targeted by inhibitors

The presence of both HDAC1-3- and HDAC8-specific loops in the tcDAC2 active site clearly confers an atypical and specific character to the active site of this parasite enzyme. We previously showed that HDAC8 enzymes have a unique pocket in their active site that can specifically accommodate HDAC8-selective inhibitors and could also be employed for specific substrate recognition, which we termed the HDAC8-selective pocket (Marek et al., 2018). This pocket is composed of the catalytic tyrosine side chain at its bottom, and its walls are made up of residues from HDAC8 L1 and L6 loops.

Notably, HDAC8 active site L6 loop composition, specific conformation, and rigidity are critical for the design of HDAC8-selective inhibitors but also for the activity of this enzyme, mirroring the functional importance of this loop in other HDACs (Millard

et al., 2013; Porter and Christianson, 2019; Watson et al., 2012, 2016; Marek et al., 2018; Hai and Christianson, 2016; Miyake et al., 2016; Hai et al., 2017). The HDAC8-selective pocket exists only in HDAC8, being filled in by hydrophobic residues from the L1 and L6 loops (L1–L6 lock) in other human HDACs (Marek et al., 2018). Because of the HDAC8 character of the tcDAC2 L1 loop and the HDAC1-3 character of the tcDAC2 L6 loop, this pocket is also partially filled in tcDAC2, causing a partial L1–L6 lock (Figure 5C) and, thus, explaining that HDAC8-selective inhibitors cannot strongly inhibit tcDAC2 (Table S1).

Analysis of the tcDAC2 active site reveals, however, the presence of a unique pocket in this enzyme that is not observed in the structures of other human HDACs (Figure 5C). This pocket is located between the tcDAC2 L5 and L6 loops. The unique character of this pocket is due to the replacement of a bulky phenylalanine/tyrosine residue—observed in all human HDAC structures solved so far—by a smaller isoleucine residue (I266) in the tcDAC2 L5 loop (Figures 1, 5D, and S1B). In addition, the back of the pocket is freed by a short alanine residue (A261), replacing longer arginine or lysine residues in human HDAC structures, and is overlooked on the side opposite the active site zinc by a long glutamate residue replacing generally shorter residues in human HDACs (Figures 1, 5D, and S1B).

We next analyzed the binding mode of the QSN and TB56 HDAC inhibitors to tcDAC2. Both inhibitors bind in the tcDAC2 active site with their hydroxamate warhead coordinating the catalytic zinc, interacting with the hydroxyl group of Y371 catalytic tyrosine and with both histidines H197 and H198 (Figure 6), as observed in many HDAC/hydroxamate inhibitor-containing structures. The rigid linker of QSN binds into the hydrophobic channel formed by F207, F267, and L6 loop L335, with its capping group stacking on top of the L5 loop, notably F267 (Figure 6A). However, QSN does not interact with residues of the tcDAC2-unique pocket. This is different for TB56, whose dibenzofuran moiety also binds into the pocket formed by F207, F267, and L6 loop L335 but also occupies the entrance of the tcDAC2-unique pocket (Figure 6B). This demonstrates that the tcDAC2-unique pocket can be targeted to develop novel inhibitors that could be selective for this trypanosome enzyme.

Not only the active site, but also the foot pocket at the base of HDAC active sites, can be targeted by inhibitors. In hsHDAC1-3, this pocket is reduced in size due to various hydrophobic residues that fill it in, while in hsHDAC8, its size can change according to the conformations adopted by tyrosine Y111 and tryptophan W141. Interestingly, in tcDAC2, an arginine (R196) is found in replacement of hsHDAC8 W141 and the equivalent leucine in hsHDAC1-3, thus increasing the charged character of this foot pocket that could also be used to selectively target tcDAC2. The unique character of the tcDAC2 foot pocket could also explain why the benzamide-based HDAC1-3-selective inhibitors (Mocetinostat, Entinostat), which bind selectively into this pocket, perform poorly in our inhibition studies (Table S1).

(C) Surface representation of the active site of the three enzymes. The conformation of tcDAC2 L6 loop causes an L1–L6 lock that prevents the formation of a selective and functionally important pocket observed in HDAC8 (Marek et al., 2018). In contrast, tcDAC2 has a unique pocket formed between its L5 and L6 loops that does not exist in human HDACs due to an L5–L6 lock.

(D) Residues forming the tcDAC2-unique pocket. This pocket is created by the replacement by small residues in tcDAC2 of larger residues found in other HDACs.

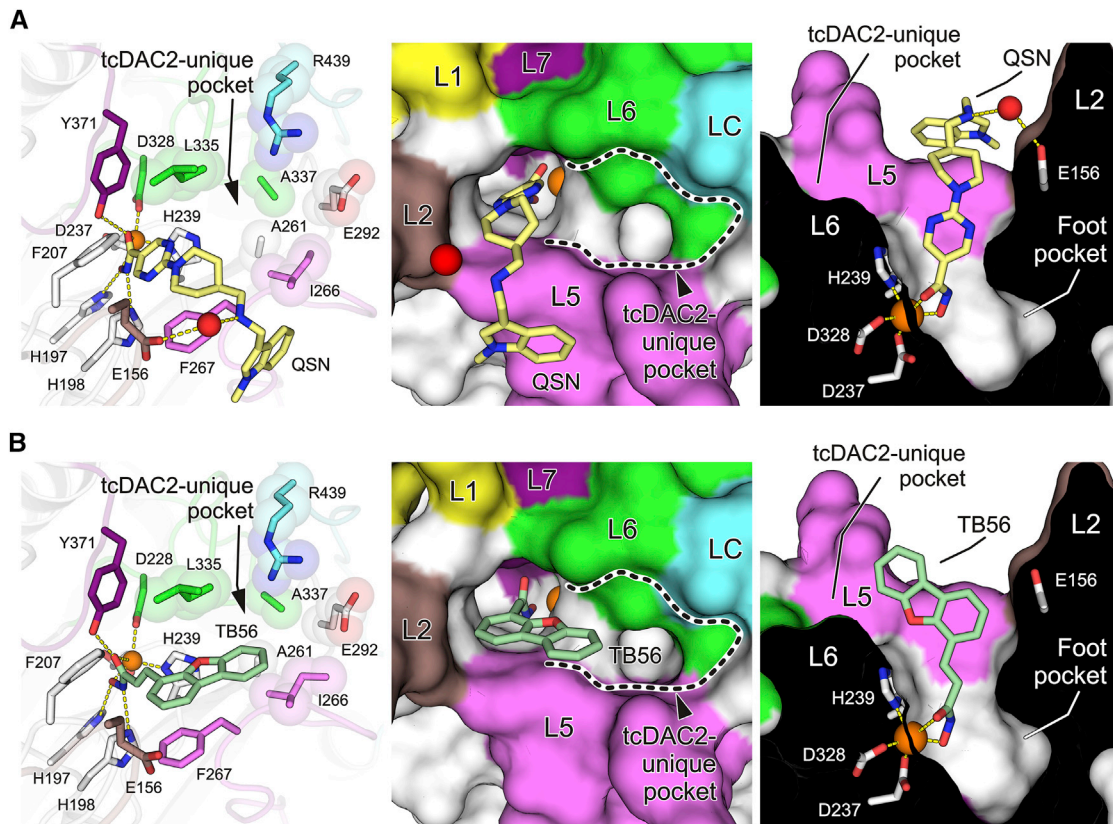


Figure 6. Molecular basis of inhibition of tcDAC2 by QSN and TB56

Binding of inhibitors in the tcDAC2 active site using residues (left panels), surface (middle panels), and pocket (right panels) views.

(A) Binding of Quisinostat (QSN) to tcDAC2. The QSN inhibitor shows a canonical binding mode, as observed for many pan-HDAC inhibitors bound to different HDACs.

(B) Binding of TB56 to tcDAC2. TB56 occupies the entrance of the tcDAC2-unique pocket, demonstrating the potential of this pocket to accommodate tcDAC2-selective inhibitors.

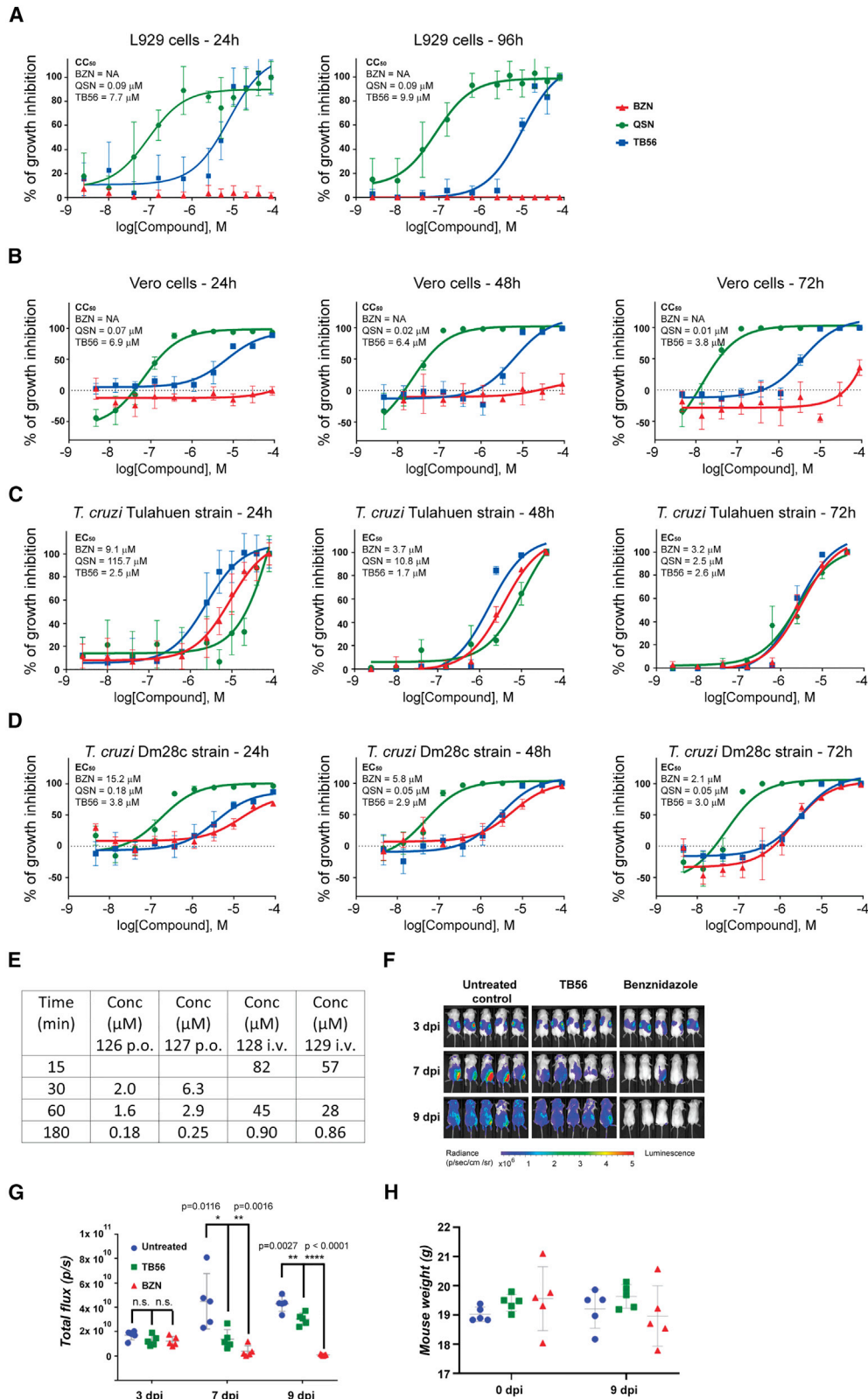
Anti-parasitic effects of inhibitors

We next investigated the effects of QSN and the tcDAC2-specific pocket-targeting compound TB56, together with the anti-trypansomore drug BZN, in *in cellulo* infection models using two previously validated protocols using different cell lines and two different *T. cruzi* strains (Buckner et al., 1996; MacLean et al., 2018; Romanha et al., 2010). Specifically, these protocols made use of (1) the *T. cruzi* Tulahuen strain infecting L929 cells with an indirect readout determining the β -galactosidase activity and (2) the *T. cruzi* Dm28c strain infecting Vero cells using a direct high-content image-based readout.

Cytotoxicity assays were performed at different time points for both protocols and revealed that BZN has no effect on L929 cells and only very little toxicity on Vero cells, as previously reported (Araujo-Lima et al., 2018; MacLean et al., 2018; Martín-Escolano et al., 2018) (Figures 7A and 7B). In contrast, QSN showed significant cytotoxicity (CC_{50} in the range of 0.01–0.09 μ M) for both cell lines, in agreement with recently reported cytotoxicity assays for different cell lines (Morales Torres et al., 2020). TB56 showed a lower cytotoxicity than QSN, with CC_{50} values ranging between 3.8 and 9.9 μ M, depending on the cell line (Figures 7A and 7B).

We next tested the effect of the three compounds on the *T. cruzi* parasite in infected cells using three readout time points (24, 48, and 72 h) (Figures 7C, 7D, and S7). Later time points were not used since the infected cells start to be lysed by the parasites after 72 h. In these assays, BZN showed EC_{50} values between 2.1 and 15.2 μ M for both *T. cruzi* strains. Similarly, TB56 showed EC_{50} values in the range of 1.7–3.8 μ M on both *T. cruzi* strains. Importantly, we observed in our high-content image-based experiments that TB56 is more toxic to the parasite than to the cells when kept at sufficiently low concentration (3.3 μ M; Figures S7D and S7E). These assays, therefore, indicated that TB56 represents a potentially promising anti-parasitic lead compound.

In contrast to BZN and TB56, the EC_{50} values measured for QSN were different depending on the protocol used, with values in the range of 2.5–115.7 μ M for the Tulahuen strain and 0.05–0.18 μ M for the Dm28c strain (Figures 7C and 7D). Further contrasting with the two other compounds, even when the EC_{50} values of QSN were close to the CC_{50} for the infection of Vero cells by the Dm28c strain, our high-content image-based assays showed that QSN is more toxic to the cells than to the *T. cruzi* strain (Figures S7C and S7E). Therefore, in contrast to its potential use for treating cancer cells reported recently (Morales Torres



(legend on next page)

et al., 2020), QSN appears less suited as a potential anti-Chagas disease agent.

The positive results obtained with TB56 prompted us to investigate this compound further in a mouse infection model in comparison with BZN. We first carried out a pharmacokinetic study to assess the TB56 dose to be used. We administered 50 mg/kg TB56 to two male mice intravenously (i.v.) and to two male mice orally by gavage (p.o.). The doses were well tolerated, and we observed during the first hour a high TB56 plasma concentration with i.v. administration and a moderate TB56 plasma concentration with p.o. administration (Figure 7E). However, the plasma concentrations decreased rapidly to below 1 μ M at 3 h post-administration. A TB56 dose of 50 mg/kg/day was chosen for the mouse infection model.

While the mice treated with BZN recovered fully at 9 days post-infection (dpi), the mice treated with TB56 showed a significant reduction in parasite load at 7 dpi compared to the control group, but much less at 9 dpi, showing that TB56 had an effect but could not fully stop the infection (Figures 7F–7H). The TB56 plasma concentration decrease observed during the pharmacokinetic study could explain the milder effect of TB56 in these *in vivo* assays. Nevertheless, although TB56 does not reach the same level of *in vivo* efficacy as observed with the drug BZN, it shows a potential as a starting lead compound for the development of new drugs against *T. cruzi* and paves the way for the design of inhibitors binding into the tcDAC2-unique pocket.

DISCUSSION

The fight against eukaryotic parasites remains a major health issue when no vaccine and only a few drugs are available to treat them. We have previously shown that targeting the epigenetic machinery of eukaryotic pathogens through repurposing and piggyback strategies represents a valid approach to tackle this issue, although selectivity has to be addressed (Bayer et al., 2018; Heimburg et al., 2016, 2017; Marek et al., 2013, 2015,

2018; Schiedel et al., 2015; Monaldi et al., 2019). Here, we have used a similar approach to target HDACs from the eukaryotic flagellate *Trypanosoma cruzi* that causes tens of thousands of deaths yearly. Our study shows that trypanosome HDACs could be bona fide anti-parasitic drug targets, as they have evolved specific features that should facilitate addressing the selectivity issue.

Specifically, our structure of tcDAC2 shows major changes in its C-terminal part that distinguish this enzyme from human HDACs and define specific structural elements at its surface that could be used by tcDAC2 to interact with specific partners and targets. This specificity is reinforced by tcDAC2 insertions 1 and 2 and the absence of an arginine in its L6 loop, which prevent interactions being made with partners, as observed for the human HDAC1/MTA1 and HDAC3/NCoR complexes (Millard et al., 2013; Watson et al., 2012, 2016), or by the unique positioning of the tcDAC2 α C-helix. Thus, the atypical character of tcDAC2 suggested by the initial phylogenetic analyses is confirmed at the structural level.

The specific character of tcDAC2 is also found in the organization of its active site. While most of the loops that form the tcDAC2 active site adopt a conformation close to that of HDAC8 loops, the L6 loop conformation is highly similar to that observed for the HDAC1-3 isozyme family. However, in contrast to the tcDAC2 C-terminal half, whose structure has evolved specific features, tcDAC2 active site loops still retain canonical structural features as observed in human HDACs; only the combination of the loops is different and creates specificity. This modularity of the tcDAC2 active site raises the question of target recognition by tcDAC2: one possibility is that tcDAC2 deacetylates several targets that are normally processed by different HDACs in humans.

Another non-mutually exclusive possibility would be that the combination of these different loops creates a surface that recognizes a completely different sequence motif specific to *T. cruzi* proteins. Accordingly, we observe the presence in the

Figure 7. Inhibition of *T. cruzi* in cellular and mice infection models

- (A) Dose-response curves obtained from L929 cells treated with Benznidazole (BZN), QSN, and TB56 for 24 and 96 h. BZN does not show toxicity to L929 cells with the concentrations used in these assays. The toxicity values (CC_{50}) for BZN, QSN, and TB56 are indicated in the figure.
- (B) Dose-response curves obtained from Vero cells treated with BZN, QSN, and TB56 for 24, 48, and 72 h. The toxicity values (CC_{50}) for BZN, QSN, and TB56 are indicated in the figure. BZN shows very little toxicity, while TB56 shows the same toxicity as for the L929 cells. QSN shows higher cytotoxicity than for the L929 cells.
- (C) Dose-response curves of *T. cruzi* Tulahuen strain inhibition obtained from infected L929 cell cultures treated with BZN, QSN, and TB56 for 24, 48, and 72 h. The respective EC_{50} values are indicated in the figure.
- (D) Dose-response curves obtained from Vero cell cultures infected by the *T. cruzi* Dm28c strain treated with BZN, QSN, and TB56 for 24, 48, and 72 h. The respective EC_{50} values are indicated in the figure.
- (E) Results of the pharmacokinetic study showing the TB56 concentration versus time in mouse plasma samples after administration of 50 mg/kg TB56 p.o. (mouse 126 and 127) or i.v. (mouse 128 and 129).
- (F) Analysis of *T. cruzi* infection in a mouse model. *In vivo* luminescence images are shown for the untreated control group (left), the group treated with TB56 (center), and the group treated with BZN (right) acquired at 3 days post infection (dpi), before the treatment started, and at 7 and 9 dpi, respectively, after 3 and 5 days of treatment with the indicated compounds. A visual reduction of luminescence levels can be observed both for TB56- and BZN-treated mice.
- (G) Luminescence quantification of the images shown in (F), confirming a significant inhibition of *T. cruzi* in TB56-treated mice relative to the control group at 7 dpi, albeit weaker than for the BZN-treated mice.
- (H) Weight of the mice used and reported in (F) and (G) measured at the start and at the end of the experiment (0 and 9 dpi). The differences observed are statistically non-significant.

All assays in (A)–(D) were performed with two to six biological replicates tested in technical quadruplicates (A), one to five biological replicates tested in technical quadruplicates (C), and technical quadruplicates (B and D). In (A)–(D), data are represented as mean \pm SD. In (G) and (H), data are shown for each individual mouse, represented by an individual symbol, and the mean and SD are represented, respectively, as light gray horizontal and vertical lines, $n = 5$. p values were calculated using one-way ANOVA with spherical data and Tukey's multiple tests.

tcDAC2 active site of a unique pocket that potentially does not exist in human HDACs. This pocket recalls the unique pocket found in HDAC8 that appears important for HDAC8 activity (Marek et al., 2018). Importantly, reminiscent of the HDAC8-selective pocket, the tcDAC2-unique pocket could be used to develop selective inhibitors to fight Chagas disease.

Specifically, we show that one inhibitor used in our study can partially occupy this pocket (Video S1) and shows anti-parasitic effects in *in cellulo* and *in vivo* models of infection. Although the *in vivo* effects are surpassed by the Chagas-disease-approved drug BZN, the fact that our compound has potency in the low micromolar range and is rapidly degraded *in vivo* leaves room for the development of novel stable drug candidates. The fact that it does not make use of the full interaction potential of the tcDAC2-unique pocket potentially explains its reduced selectivity and provides a clear path for structure-guided improvement. Other hydroxamic-acid-based HDAC inhibitors are approved for therapy of human diseases, which shows that the pharmacokinetic weakness can be overcome in this class of inhibitors.

Thus, tcDAC2 represents an important target to develop new drugs against *T. cruzi* since this enzyme is functionally essential to the parasite, in contrast to the *T. brucei* tbDAC2 homolog. Importantly, analysis of the conservation of active site residues in different trypanosome species shows that most of them have a DAC2 enzyme that resembles tcDAC2 and not tbDAC2 (Table S3). DAC2, therefore, also represents a potential therapeutic target in these other trypanosome species. More generally, our results show that the different trypanosome HDACs, due to their atypical character, could also be used as drug targets. Most importantly, this also applies to the other major pathogens causing leishmaniasis and malaria that harbor evolutionarily distinct zinc-dependent HDACs (Scholte et al., 2017) but whose structures still remain unknown. Therefore, our work opens new avenues toward the species-specific targeting of eukaryotic pathogens.

Limitations of the study

Two common potential technical limitations of our study concern its structural and chemical inhibition analyses. First, the reported structural analyses could be impacted by the molecular interactions within the protein crystals. The comparison between our two unrelated crystal forms with totally different crystal packings, however, supports the robustness of the conclusions drawn. Second, we cannot exclude off-target effects of the inhibitors tested when performing *in cellulo* and *in vivo* studies. More generally, epigenetic mechanisms are essential to the life cycle of many pathogens, and targeting of epigenetic effectors represents an important field of the anti-parasitic investigations. The current study does not address the involvement of tcDAC2 in epigenetic mechanisms. This will require the dedicated identification of its specific targets, which may reveal, considering the small number of HDACs in trypanosomes, a dual involvement in both epigenetic and non-epigenetic mechanisms. Similarly, this study does not address the question of whether tcDAC2 possesses a deacetylation activity or a deacylation activity, or even a dual deacetylation/deacylation activity *in vivo*. This will also require the independent iden-

tification of tcDAC2 substrates, as well as their posttranslational modifications.

STAR★METHODS

Detailed methods are provided in the online version of this paper and include the following:

- KEY RESOURCES TABLE
- RESOURCE AVAILABILITY
 - Lead contact
 - Materials availability
 - Data and code availability
- EXPERIMENTAL MODEL AND SUBJECT DETAILS
 - *In vivo* animal studies
 - Cell lines and microbe strains
 - Organisms
- METHOD DETAILS
 - Sequence comparisons
 - Gene targeted deletion by homologous recombination
 - Gene targeted deletion mediated by CRISPR-Cas9
 - tcDAC2 complementation assays
 - Cell cycle analysis
 - Morphological characterization
 - Cell proliferation analysis
 - Molecular cloning and mutagenesis
 - Large-scale production of tcDAC2
 - TB compounds synthesis
 - tcDAC2 activity and inhibition assays
 - hsHDAC1/6 activity and inhibition assays
 - hsHDAC8 activity and inhibition assays
 - Dynamic light scattering
 - Differential scanning fluorimetry
 - Limited proteolysis assay
 - Protein crystallization experiments and data collection
 - Structure determination and refinement
 - Determination of cytotoxicity on L929 cells
 - L929 cell infection assays
 - Intracellular *T. cruzi* inhibition in infected Vero cells
 - Pharmacokinetic study
 - Mouse infection assays
- QUANTIFICATION AND STATISTICAL ANALYSIS

SUPPLEMENTAL INFORMATION

Supplemental information can be found online at <https://doi.org/10.1016/j.celrep.2021.110129>.

ACKNOWLEDGMENTS

This work and the authors of this manuscript have been supported by funding from the European Union's Seventh Framework Programme for research, technological development, and demonstration under grant agreement no. 602080 (A-ParaDDisE). C.R., M.M., E.R.-M., and T.B.S. were supported by institutional funds from the Centre National de la Recherche Scientifique (CNRS), the Institut National de la Santé et de la Recherche Médicale (INSERM), and the Université de Strasbourg. C.R. acknowledges the support by the Fondation ARC. R.J.P. was supported by institutional funds from the CNRS, the Institut Pasteur de Lille, and Lille University. N.I.T.Z., G.F.A.P.-C., E.P.G.-S., and M.M.M. were partially supported by the Brazilian National

Research Council (CNPq), the Research Foundation from the state of Paraná (FapPR), and the INOVA research program from FIOCRUZ. The authors acknowledge the support and the use of resources of the French Infrastructure for Integrated Structural Biology FRISBI ANR-10-INBS-05 and of Instruct-ERIC. The authors thank the Program for Technological Development of Tools for Health-PDTIS-FIOCRUZ for the use of its facilities. W.S. and K.H. acknowledge the financial support by the European Regional Development Fund of the European Commission. M.J. and A.M. were supported by the Deutsche Forschungsgemeinschaft – Project ID 192904750 – CRC 992 Medical Epigenetics. We wish to thank members of the Swiss Light Source (SLS) and SOLEIL synchrotrons for the use of their beamline facilities and for help during data collection.

AUTHOR CONTRIBUTIONS

M.M., E.R.-M., and G.F.A.P.-C. contributed equally to this work. M.M., E.R.-M., T.B.S., E.T., and C.R. performed all the biochemical, biophysical, and structural studies. G.F.A.P.-C., E.P.G.-S., and N.I.T.Z. performed the *T. cruzi* gene deletion and genetic complementation studies, the *in cellulo* high-content image-based experiments, and the mice infection assays. P.A.S.-J. and M.M.M. performed the *in cellulo* assays based on indirect readout of β -galactosidase activity. T.B., K.H., and W.S. synthesized the tested inhibitors, did the analytical characterizations, and carried out the docking studies. D.H., A.M., A.C., K.S., and M.J. performed the enzymatic activity and inhibition assays and analyzed these data. C.N. and J.S. performed enzymatic activity assays and the pharmacokinetic study. M.M., G.F.A.P.-C., S.G., R.J.P., M.M.M., M.J., J.S., W.S., N.I.T.Z., and C.R. designed the experiments, analyzed data, and wrote the paper.

DECLARATION OF INTERESTS

The authors declare no competing interests.

Received: July 6, 2021

Revised: October 26, 2021

Accepted: November 23, 2021

Published: December 21, 2021

SUPPORTING CITATIONS

The following references appear in the Supplemental information: Hess-Stump et al. (2007); Krieger et al. (2019); Marson et al. (2015).

REFERENCES

Andrews, K.T., Haque, A., and Jones, M.K. (2012a). HDAC inhibitors in parasitic diseases. *Immunol. Cell Biol.* **90**, 66–77.

Andrews, K.T., Tran, T.N., and Fairlie, D.P. (2012b). Towards histone deacetylase inhibitors as new antimalarial drugs. *Curr. Pharm. Des.* **18**, 3467–3479.

Andrews, K.T., Fisher, G., and Skinner-Adams, T.S. (2014). Drug repurposing and human parasitic protozoan diseases. *Int. J. Parasitol. Drugs Drug Resist.* **4**, 95–111.

Araujo-Lima, C.F., Peres, R.B., Silva, P.B., Batista, M.M., Aiub, C.A.F., Felzenszwalb, I., and Soeiro, M.N.C. (2018). Repurposing Strategy Of Atorvastatin Against *Trypanosoma Cruzi*: In Vitro Monotherapy And Combined Therapy With Benzimidazole Exhibit Synergistic Trypanocidal Activity. *Antimicrob Agents Chemother* **62**, e00978-18.

Bayer, T., Chakrabarti, A., Lancelot, J., Shaik, T.B., Hausmann, K., Melesina, J., Schmidkunz, K., Marek, M., Erdmann, F., Schmidt, M., et al. (2018). Synthesis, Crystallization Studies, And In Vitro Characterization Of Cinnamic Acid Derivatives As Smhdac8 Inhibitors For The Treatment Of Schistosomiasis. *ChemMedChem* **13**, 1517–1529.

Bonaldo, M.C., Souto-Pradon, T., de Souza, W., and Goldenberg, S. (1988). Cell-substrate adhesion during *Trypanosoma cruzi* differentiation. *J. Cell Biol.* **106**, 1349–1358.

Bradner, J.E., West, N., Grachan, M.L., Greenberg, E.F., Haggarty, S.J., Warshaw, T., and Mazitschek, R. (2010). Chemical phylogenetics of histone deacetylases. *Nat. Chem. Biol.* **6**, 238–243.

Buckner, F.S., Verlinde, C.L., La Flamme, A.C., and Van Voorhis, W.C. (1996). Efficient technique for screening drugs for activity against *Trypanosoma cruzi* using parasites expressing beta-galactosidase. *Antimicrob. Agents Chemother.* **40**, 2592–2597.

Büscher, P., Cecchi, G., Jamonneau, V., and Priotto, G. (2017). Human African trypanosomiasis. *Lancet* **390**, 2397–2409.

Camargo, E.P. (1964). Growth And Differentiation In *Trypanosoma Cruzi*. I. Origin Of Metacyclic Trypanosomes In Liquid Media. *Rev. Inst. Med. Trop. São Paulo* **6**, 93–100.

Campo, V.A. (2017). Comparative effects of histone deacetylases inhibitors and resveratrol on *Trypanosoma cruzi* replication, differentiation, infectivity and gene expression. *Int. J. Parasitol. Drugs Drug Resist.* **7**, 23–33.

Carrillo, A.K., Guigumde, W.A., and Guy, R.K. (2015). Evaluation of histone deacetylase inhibitors (HDACi) as therapeutic leads for human African trypanosomiasis (HAT). *Bioorg. Med. Chem.* **23**, 5151–5155.

Choudhary, C., Kumar, C., Gnad, F., Nielsen, M.L., Rehman, M., Walther, T.C., Olsen, J.V., and Mann, M. (2009). Lysine acetylation targets protein complexes and co-regulates major cellular functions. *Science* **325**, 834–840.

Choudhary, C., Weinert, B.T., Nishida, Y., Verdin, E., and Mann, M. (2014). The growing landscape of lysine acetylation links metabolism and cell signalling. *Nat. Rev. Mol. Cell Biol.* **15**, 536–550.

Contreras, V.T., Araujo-Jorge, T.C., Bonaldo, M.C., Thomaz, N., Barbosa, H.S., Meirelles, Mde.N., and Goldenberg, S. (1988). Biological aspects of the Dm 28c clone of *Trypanosoma cruzi* after metacyclogenesis in chemically defined media. *Mem. Inst. Oswaldo Cruz* **83**, 123–133.

de Souza, F.S., Rampazzo, Rde.C., Manhaes, L., Soares, M.J., Cavalcanti, D.P., Krieger, M.A., Goldenberg, S., and Fragoso, S.P. (2010). Knockout of the gene encoding the kinetoplast-associated protein 3 (KAP3) in *Trypanosoma cruzi*: effect on kinetoplast organization, cell proliferation and differentiation. *Mol. Biochem. Parasitol.* **172**, 90–98.

Desravines, D.C., Serna Martin, I., Schneider, R., Mas, P.J., Aleksandrova, N., Jensen, M.R., Blackledge, M., and Hart, D.J. (2017). Structural Characterization of the SMRT Corepressor Interacting with Histone Deacetylase 7. *Sci. Rep.* **7**, 3678.

Diebold, M.L., Fribourg, S., Koch, M., Metzger, T., and Romier, C. (2011). Deciphering correct strategies for multiprotein complex assembly by co-expression: application to complexes as large as the histone octamer. *J. Struct. Biol.* **175**, 178–188.

Drazic, A., Myklebust, L.M., Ree, R., and Arnesen, T. (2016). The world of protein acetylation. *Biochim. Biophys. Acta* **1864**, 1372–1401.

Eckschlager, T., Plich, J., Stiborova, M., and Hrabeta, J. (2017). Histone Deacetylase Inhibitors as Anticancer Drugs. *Int. J. Mol. Sci.* **18**, 1414.

Emsley, P., Lohkamp, B., Scott, W.G., and Cowtan, K. (2010). Features and development of Coot. *Acta Crystallogr. D Biol. Crystallogr.* **66**, 486–501.

Engel, J.A., Jones, A.J., Avery, V.M., Sumanadasa, S.D., Ng, S.S., Fairlie, D.P., Skinner-Adams, T., and Andrews, K.T. (2015). Profiling the anti-protozoal activity of anti-cancer HDAC inhibitors against *Plasmodium* and *Trypanosoma* parasites. *Int. J. Parasitol. Drugs Drug Resist.* **5**, 117–126.

Falkenberg, K.J., and Johnstone, R.W. (2014). Histone deacetylases and their inhibitors in cancer, neurological diseases and immune disorders. *Nat. Rev. Drug Discov.* **13**, 673–691.

Fioravanti, R., Mautone, N., Rovere, A., Rotili, D., and Mai, A. (2020). Targeting histone acetylation/deacetylation in parasites: an update (2017–2020). *Curr. Opin. Chem. Biol.* **57**, 65–74.

Fujisawa, T., and Filippakopoulos, P. (2017). Functions of bromodomain-containing proteins and their roles in homeostasis and cancer. *Nat. Rev. Mol. Cell Biol.* **18**, 246–262.

Hai, Y., and Christianson, D.W. (2016). Histone deacetylase 6 structure and molecular basis of catalysis and inhibition. *Nat. Chem. Biol.* **12**, 741–747.

- Hai, Y., Shinsky, S.A., Porter, N.J., and Christianson, D.W. (2017). Histone deacetylase 10 structure and molecular function as a polyamine deacetylase. *Nat. Commun.* **8**, 15368.
- Hailu, G.S., Robaa, D., Forgione, M., Sippl, W., Rotili, D., and Mai, A. (2017). Lysine Deacetylase Inhibitors in Parasites: Past, Present, and Future Perspectives. *J. Med. Chem.* **60**, 4780–4804.
- Heimburg, T., Chakrabarti, A., Lancelot, J., Marek, M., Melesina, J., Hauser, A.T., Shaik, T.B., Duclaud, S., Robaa, D., Erdmann, F., et al. (2016). Structure-Based Design and Synthesis of Novel Inhibitors Targeting HDAC8 from *Schistosoma mansoni* for the Treatment of Schistosomiasis. *J. Med. Chem.* **59**, 2423–2435.
- Heimburg, T., Kolbinger, F.R., Zeyen, P., Ghazy, E., Herp, D., Schmidtkunz, K., Melesina, J., Shaik, T.B., Erdmann, F., Schmidt, M., et al. (2017). Structure-Based Design and Biological Characterization of Selective Histone Deacetylase 8 (HDAC8) Inhibitors with Anti-Neuroblastoma Activity. *J. Med. Chem.* **60**, 10188–10204.
- Heltweg, B., Dequiedt, F., Marshall, B.L., Brauch, C., Yoshida, M., Nishino, N., Verdin, E., and Jung, M. (2004). Subtype selective substrates for histone deacetylases. *J. Med. Chem.* **47**, 5235–5243.
- Heltweg, B., Trapp, J., and Jung, M. (2005). In vitro assays for the determination of histone deacetylase activity. *Methods* **36**, 332–337.
- Henriques, C., Henriques-Pons, A., Meuser-Batista, M., Ribeiro, A.S., and de Souza, W. (2014). In vivo imaging of mice infected with bioluminescent *Trypanosoma cruzi* unveils novel sites of infection. *Parasit. Vectors* **7**, 89.
- Hess-Stumpp, H., Bracker, T.U., Henderson, D., and Politz, O. (2007). MS-275, a potent orally available inhibitor of histone deacetylases—the development of an anticancer agent. *Int. J. Biochem. Cell Biol.* **39**, 1388–1405.
- Holm, L. (2020). DALI and the persistence of protein shape. *Protein Sci.* **29**, 128–140.
- Hudson, G.M., Watson, P.J., Fairall, L., Jamieson, A.G., and Schwabe, J.W.R. (2015). Insights into the Recruitment of Class IIa Histone Deacetylases (HDACs) to the SMRT/NCOR Transcriptional Repression Complex. *J. Biol. Chem.* **290**, 18237–18244.
- Ingram, A.K., and Horn, D. (2002). Histone deacetylases in *Trypanosoma brucei*: two are essential and another is required for normal cell cycle progression. *Mol. Microbiol.* **45**, 89–97.
- Kabsch, W. (2010). Xds. *Acta Crystallogr. D Biol. Crystallogr.* **66**, 125–132.
- Katoh, K., Rozewicki, J., and Yamada, K.D. (2019). MAFFT online service: multiple sequence alignment, interactive sequence choice and visualization. *Brief. Bioinform.* **20**, 1160–1166.
- Kelly, J.M., Taylor, M.C., Horn, D., Loza, E., Kalvinsh, I., and Björkling, F. (2012). Inhibitors of human histone deacetylase with potent activity against the African trypanosome *Trypanosoma brucei*. *Bioorg. Med. Chem. Lett.* **22**, 1886–1890.
- Krieger, V., Hamacher, A., Cao, F., Stenzel, K., Gertzen, C.G.W., Schäker-Hübner, L., Kurz, T., Gohlke, H., Dekker, F.J., Kassack, M.U., and Hansen, F.K. (2019). Synthesis of Peptoid-Based Class I-Selective Histone Deacetylase Inhibitors with Chemosensitizing Properties. *J. Med. Chem.* **62**, 11260–11279.
- Li, Y., and Seto, E. (2016). HDACs and HDAC Inhibitors in Cancer Development and Therapy. *Cold Spring Harb. Perspect. Med.* **6**, a026831.
- Liebschner, D., Afonine, P.V., Baker, M.L., Bunkóczi, G., Chen, V.B., Croll, T.I., Hintze, B., Hung, L.W., Jain, S., McCoy, A.J., et al. (2019). Macromolecular structure determination using X-rays, neutrons and electrons: recent developments in Phenix. *Acta Crystallogr. D Struct. Biol.* **75**, 861–877.
- MacLean, L.M., Thomas, J., Lewis, M.D., Cotillo, I., Gray, D.W., and De Rycker, M. (2018). Development of *Trypanosoma cruzi* in vitro assays to identify compounds suitable for progression in Chagas' disease drug discovery. *PLoS Negl. Trop. Dis.* **12**, e0006612.
- Madeira, F., Park, Y.M., Lee, J., Buso, N., Gur, T., Madhusoodanan, N., Basutkar, P., Tivey, A.R.N., Potter, S.C., Finn, R.D., and Lopez, R. (2019). The EMBL-EBI search and sequence analysis tools APIs in 2019. *Nucleic Acids Res.* **47**, W636–W641.
- Mandava, V., Fernandez, J.P., Deng, H., Janzen, C.J., Hake, S.B., and Cross, G.A. (2007). Histone modifications in *Trypanosoma brucei*. *Mol. Biochem. Parasitol.* **156**, 41–50.
- Marek, M., Kannan, S., Hauser, A.T., Moraes Mourão, M., Caby, S., Cura, V., Stolfa, D.A., Schmidtkunz, K., Lancelot, J., Andrade, L., et al. (2013). Structural basis for the inhibition of histone deacetylase 8 (HDAC8), a key epigenetic player in the blood fluke *Schistosoma mansoni*. *PLoS Pathog.* **9**, e1003645.
- Marek, M., Oliveira, G., Pierce, R.J., Jung, M., Sippl, W., and Romier, C. (2015). Drugging the schistosome zinc-dependent HDACs: current progress and future perspectives. *Future Med. Chem.* **7**, 783–800.
- Marek, M., Shaik, T.B., Heimburg, T., Chakrabarti, A., Lancelot, J., Ramos-Morales, E., Da Veiga, C., Kalinin, D., Melesina, J., Robaa, D., et al. (2018). Characterization of Histone Deacetylase 8 (HDAC8) Selective Inhibition Reveals Specific Active Site Structural and Functional Determinants. *J. Med. Chem.* **61**, 10000–10016.
- Marmorstein, R., and Zhou, M.M. (2014). Writers and readers of histone acetylation: structure, mechanism, and inhibition. *Cold Spring Harb. Perspect. Biol.* **6**, a018762.
- Marson, C.M., Matthews, C.J., Atkinson, S.J., Lamadema, N., and Thomas, N.S. (2015). Potent and Selective Inhibitors of Histone Deacetylase-3 Containing Chiral Oxazoline Capping Groups and a N-(2-Aminophenyl)-benzamide Binding Unit. *J. Med. Chem.* **58**, 6803–6818.
- Martín-Escolano, R., Moreno-Viguri, E., Santivañez-Veliz, M., Martín-Montes, A., Medina-Carmona, E., Paucar, R., Marín, C., Azqueta, A., Cirauqui, N., Pey, A.L., et al. (2018). Second Generation of Mannich Base-Type Derivatives with in Vivo Activity against *Trypanosoma cruzi*. *J. Med. Chem.* **61**, 5643–5663.
- McCoy, A.J., Grosse-Kunstleve, R.W., Adams, P.D., Winn, M.D., Storoni, L.C., and Read, R.J. (2007). Phaser crystallographic software. *J. Appl. Cryst.* **40**, 658–674.
- Millard, C.J., Watson, P.J., Celardo, I., Gordiyenko, Y., Cowley, S.M., Robinson, C.V., Fairall, L., and Schwabe, J.W. (2013). Class I HDACs share a common mechanism of regulation by inositol phosphates. *Mol. Cell* **51**, 57–67.
- Miyake, Y., Keusch, J.J., Wang, L., Saito, M., Hess, D., Wang, X., Melancon, B.J., Helquist, P., Gut, H., and Matthias, P. (2016). Structural insights into HDAC6 tubulin deacetylation and its selective inhibition. *Nat. Chem. Biol.* **12**, 748–754.
- Monaldi, D., Rotili, D., Lancelot, J., Marek, M., Wössner, N., Lucidi, A., Tomasselli, D., Ramos-Morales, E., Romier, C., Pierce, R.J., et al. (2019). Structure-Reactivity Relationships on Substrates and Inhibitors of the Lysine Deacetylase Sirtuin 2 from *Schistosoma mansoni* (*SmSirt2*). *J. Med. Chem.* **62**, 8733–8759.
- Morales Torres, C., Wu, M.Y., Hobor, S., Wainwright, E.N., Martin, M.J., Patel, H., Grey, W., Grönroos, E., Howell, S., Carvalho, J., et al. (2020). Selective inhibition of cancer cell self-renewal through a Quisinosat-histone H1.0 axis. *Nat. Commun.* **11**, 1792.
- Moretti, N.S., Cestari, I., Anupama, A., Stuart, K., and Schenkman, S. (2018). Comparative Proteomic Analysis of Lysine Acetylation in Trypanosomes. *J. Proteome Res.* **17**, 374–385.
- Narita, T., Weinert, B.T., and Choudhary, C. (2019). Functions and mechanisms of non-histone protein acetylation. *Nat. Rev. Mol. Cell Biol.* **20**, 156–174.
- Nunez, R. (2001). DNA measurement and cell cycle analysis by flow cytometry. *Curr. Issues Mol. Biol.* **3**, 67–70.
- Park, S.Y., Kim, G.S., Hwang, H.J., Nam, T.H., Park, H.S., Song, J., Jang, T.H., Lee, Y.C., and Kim, J.S. (2018). Structural basis of the specific interaction of SMRT corepressor with histone deacetylase 4. *Nucleic Acids Res.* **46**, 11776–11788.
- Pavani, R.S., da Silva, M.S., Fernandes, C.A., Morini, F.S., Araujo, C.B., Fontes, M.R., Sant'Anna, O.A., Machado, C.R., Cano, M.I., Fragoso, S.P., and Elias, M.C. (2016). Replication Protein A Presents Canonical Functions and Is Also Involved in the Differentiation Capacity of *Trypanosoma cruzi*. *PLoS Negl. Trop. Dis.* **10**, e0005181.
- Peng, D., and Tarleton, R. (2015). EuPaGDT: a web tool tailored to design CRISPR guide RNAs for eukaryotic pathogens. *Microb. Genom.* **1**, e000033.
- Pérez-Molina, J.A., and Molina, I. (2018). Chagas disease. *Lancet* **391**, 82–94.

- Pettersen, E.F., Goddard, T.D., Huang, C.C., Couch, G.S., Greenblatt, D.M., Meng, E.C., and Ferrin, T.E. (2004). UCSF Chimera—a visualization system for exploratory research and analysis. *J. Comput. Chem.* **25**, 1605–1612.
- Picchi, G.F., Zulkievicz, V., Krieger, M.A., Zanchin, N.T., Goldenberg, S., and de Godoy, L.M. (2017). Post-translational Modifications of *Trypanosoma cruzi* Canonical and Variant Histones. *J. Proteome Res.* **16**, 1167–1179.
- Porter, N.J., and Christianson, D.W. (2019). Structure, mechanism, and inhibition of the zinc-dependent histone deacetylases. *Curr. Opin. Struct. Biol.* **59**, 9–18.
- Robert, X., and Gouet, P. (2014). Deciphering key features in protein structures with the new ENDscript server. *Nucleic Acids Res.* **42**, W320–4.
- Romagnoli, B.A.A., Picchi, G.F.A., Hiraiwa, P.M., Borges, B.S., Alves, L.R., and Goldenberg, S. (2018). Improvements in the CRISPR/Cas9 system for high efficiency gene disruption in *Trypanosoma cruzi*. *Acta Trop.* **178**, 190–195.
- Romanha, A.J., Castro, S.L., Soeiro, Mde.N., Lannes-Vieira, J., Ribeiro, I., Talvani, A., Bourdin, B., Blum, B., Olivieri, B., Zani, C., et al. (2010). In vitro and in vivo experimental models for drug screening and development for Chagas disease. *Mem. Inst. Oswaldo Cruz* **105**, 233–238.
- Sabari, B.R., Zhang, D., Allis, C.D., and Zhao, Y. (2017). Metabolic regulation of gene expression through histone acylations. *Nat. Rev. Mol. Cell Biol.* **18**, 90–101.
- Scarim, C.B., Jornada, D.H., Chelucci, R.C., de Almeida, L., Dos Santos, J.L., and Chung, M.C. (2018). Current advances in drug discovery for Chagas disease. *Eur. J. Med. Chem.* **155**, 824–838.
- Schiedel, M., and Conway, S.J. (2018). Small molecules as tools to study the chemical epigenetics of lysine acetylation. *Curr. Opin. Chem. Biol.* **45**, 166–178.
- Schiedel, M., Marek, M., Lancelot, J., Karaman, B., Almlöf, I., Schultz, J., Sippl, W., Pierce, R.J., Romier, C., and Jung, M. (2015). Fluorescence-based screening assays for the NAD⁺-dependent histone deacetylase smSirt2 from *Schistosoma mansoni*. *J. Biomol. Screen.* **20**, 112–121.
- Scholte, L.L.S., Mourão, M.M., Pais, F.S., Melesina, J., Robaa, D., Volpini, A.C., Sippl, W., Pierce, R.J., Oliveira, G., and Nahum, L.A. (2017). Evolutionary relationships among protein lysine deacetylases of parasites causing neglected diseases. *Infect. Genet. Evol.* **53**, 175–188.
- Seto, E., and Yoshida, M. (2014). Erasers of histone acetylation: the histone deacetylase enzymes. *Cold Spring Harb. Perspect. Biol.* **6**, a018713.
- Varikuti, S., Jha, B.K., Volpedo, G., Ryan, N.M., Halsey, G., Hamza, O.M., McGwire, B.S., and Satoskar, A.R. (2018). Host-Directed Drug Therapies for Neglected Tropical Diseases Caused by Protozoan Parasites. *Front. Microbiol.* **9**, 2655.
- Verdin, E., and Ott, M. (2015). 50 years of protein acetylation: from gene regulation to epigenetics, metabolism and beyond. *Nat. Rev. Mol. Cell Biol.* **16**, 258–264.
- Vincentelli, R., and Romier, C. (2016). Complex Reconstitution and Characterization by Combining Co-expression Techniques in *Escherichia coli* with High-Throughput. *Adv. Exp. Med. Biol.* **896**, 43–58.
- Wang, Q.P., Kawahara, T., and Horn, D. (2010). Histone deacetylases play distinct roles in telomeric VSG expression site silencing in African trypanosomes. *Mol. Microbiol.* **77**, 1237–1245.
- Wang, Q., Rosa, B.A., Nare, B., Powell, K., Valente, S., Rotili, D., Mai, A., Marshall, G.R., and Mitreva, M. (2015). Targeting Lysine Deacetylases (KDACs) in Parasites. *PLoS Negl. Trop. Dis.* **9**, e0004026.
- Watson, P.J., Fairall, L., Santos, G.M., and Schwabe, J.W.R. (2012). Structure of HDAC3 bound to co-repressor and inositol tetrakisphosphate. *Nature* **487**, 335–340.
- Watson, P.J., Millard, C.J., Riley, A.M., Robertson, N.S., Wright, L.C., Godage, H.Y., Cowley, S.M., Jamieson, A.G., Potter, B.V., and Schwabe, J.W. (2016). Insights into the activation mechanism of class I HDAC complexes by inositol phosphates. *Nat. Commun.* **7**, 11262.
- Williams, C.J., Headd, J.J., Moriarty, N.W., Prisant, M.G., Videau, L.L., Deis, L.N., Verma, V., Keedy, D.A., Hintze, B.J., Chen, V.B., et al. (2018). MolProbity: More and better reference data for improved all-atom structure validation. *Protein Sci.* **27**, 293–315.
- Zuma, A.A., and de Souza, W. (2018). Histone deacetylases as targets for anti-trypanosomal drugs. *Future Sci. OA* **4**, FSO325.

STAR★METHODS

KEY RESOURCES TABLE

REAGENT or RESOURCE	SOURCE	IDENTIFIER
Bacterial and virus strains		
<i>Escherichia coli</i> BL21(DE3)	Invitrogen	Cat#C600003
DH5 α	Invitrogen	Cat#18265017
Chemicals, peptides, and recombinant proteins		
Hygromycin B	GIBCO	Cat#10687010
G418	GIBCO	Cat#10131027
Trizma Base	Sigma	Cat#T1503-1KG
Blasticidin	GIBCO	Cat#A1113903
RPMI 1640	GIBCO	Cat#31800022
PBS	Invitrogen	Cat#003002
RNase A	Sigma	Cat#R5503
Propidium iodide	Invitrogen	Cat#P3566
Panotico	Laborclin	Cat#620529
NdeI	New England Biolabs	Cat#R0111S
BamHI	New England Biolabs	Cat#R0136S
Ampicillin	Sigma	Cat#A9393-25G
LB Broth medium	Sigma	Cat#L3022-1KG
Isopropyl-1-thio- β -D-galactopyranoside (IPTG)	Sigma	Cat#I6758-1G
Fetal Bovine Serum (FBS)	GIBCO	Cat#12657029
KCl	Fluka	Cat#P3911-500G
Talon Superflow Metal Affinity Resin	Merck	Cat#GE28-9574-99
TCEP	Sigma	Cat#C4706-10G
Aluminum sheets coated with Silica gel 60 F254	Merck	Cat#1055540001
CHCl ₃	Sigma-Aldrich	Cat#650498
Formic acid	Sigma-Aldrich	Cat#F0507
MeOH	Sigma-Aldrich	Cat#82762
CDCl ₃	Sigman-Aldrich	Cat#151823
DMSO-d ₆	Sigma-Aldrich	Cat#151874
Liver Infusion Tryptose (LIT) medium	Prepared in house	(Camargo, 1964)
Piperidine	Sigma-Aldrich	Cat#8.22299
PyBOP	Sigma-Aldrich	Cat#8.51009
DIPEA	Sigma-Aldrich	Cat#D125806
H ₂ NOTHP	Synthesized in house	(Heimburg et al., 2016)
NaHCO ₃	Sigma-Aldrich	Cat#S8875
MgSO ₄	Sigma-Aldrich	Cat#M3409
Et ₃ N	Sigma-Aldrich	Cat#8.08352
HCOOH	Sigma-Aldrich	Cat#F0507
Ac-Leu-Gly-(TFA)Lys-AMC	Synthesized in house	(Bradner et al., 2010)
Z-(F ₃ Ac)Lys-AMC	Synthesized in house	(Heltweg et al., 2004)
AreaPlate-96 F microplates	PerkinElmer	Cat#6005540
KH ₂ PO ₄	Sigma	Cat#P5655-100G
DMSO	Sigma	Cat#D2650
Trichostatin A	Sigma	Cat#T8552-1MG

(Continued on next page)

<i>Continued</i>		
REAGENT or RESOURCE	SOURCE	IDENTIFIER
Trypsin	Sigma	Cat#T0303-1G
HDAC1	BPS Bioscience	Cat#50051
HDAC6	BPS Bioscience	Cat#50006
Bovine Serum Albumine (BSA)	Sigma	Cat#A7030-10G
OptiPlate TM-96 F black microplates	PerkinElmer	Cat#6005279
Swissci 48-Well MRC Maxi Optimization Plates	Molecular Dimensions	Cat#MD11-004-10
Swissci 96-Well MRC Maxi Optimization Plates	Molecular Dimensions	Cat#MD11-00-10
Glycerol	Sigma	Cat#G9012-100ML
PEG200	Sigma	Cat#P3015-250G
Glutamine	GIBCO	Cat#21051024
alamarBlue	Invitrogen	Cat#DAL1100
Chlorophenol red β -D-galactopyranoside	Roche	Cat#10884308001
Benznidazole	Sigma	Cat#419656
DMEM low glucose medium	GIBCO	Cat#31600034
Penicillin-Streptomycin	GIBCO	Cat#15140148
Paraformaldehyde	Sigma	Cat#P6148
Evan's Blue	Sigma	Cat#E2129
DAPI	Sigma	Cat#D9542
(2-Hydroxypropyl)- β -cyclodextrin	Sigma	Cat#332607
DPBS	GIBCO	Cat#21600010
Propranolol	Sigma	Cat#40543
Acetonitrile	Sigma	Cat#34851
D-luciferin	Biovision	Cat#7903-100
Quisinostat	Euromedex	Cat#S1096
NP40 (Nonidet P-40)	Sigma	Cat#74385
TB51	Synthesized, this paper	N/A
TB56	Synthesized, this paper	N/A
TB72	Synthesized, this paper	N/A
TB75	Synthesized, this paper	N/A
Mocetinostat	Selleck Chemicals	S1122
Entinostat	Selleck Chemicals	S1053
NCC-149	MedKoo Biosciences	Cat#407293
Vorinostat (SAHA)	Clinisciences	HY-10221-250MG
PCI-34051	Selleck Chemicals	S2012
<i>Critical commercial assays</i>		
MEGAscript T7 kit	Invitrogen	Cat#AM1354
Fluor de Lys drug discovery kit	Enzo Life Sciences	Cat#BML-KI178
<i>Deposited data</i>		
Crystallographic structures	<u>PDB</u>	PDB: 7Q1B, 7Q1C
<i>Experimental models: Cell lines</i>		
Mouse L929 Fibroblasts	ATCC	NCTC clone 929 [L cell, L-929, derivative of Strain L]; Cat#CCL-1
Vero cells	ATCC	Cat#CCL-81
<i>Experimental models: Organisms/strains</i>		
<i>Trypanosoma cruzi</i> Tuhauen strain	Provided by Frederick S. Buckner, from University of Washington.	Tuhauen LacZ clone C4

(Continued on next page)

Continued

REAGENT or RESOURCE	SOURCE	IDENTIFIER
<i>Trypanosoma cruzi</i> Cas9-GFP expressing strain	Previous work from G. Picchi-Constante team	(Romagnoli et al., 2018)
<i>Trypanosoma cruzi</i> Dm28c strain	Stock from Fiocruz Paraná	(Contreras et al., 1988)
NMRI mice	Charles River Laboratories	https://www.criver.com/products-services/find-model/nmri-mouse
Balb/C mice	Provided by Laboratory of Animal Models, from Fiocruz Paraná	N/A
<i>Trypanosoma cruzi</i> Dm28c strain expressing firefly luciferase	Provided by Wanderley de Souza lab, from UFRJ	(Henriques et al., 2014)
Oligonucleotides		
Oligonucleotides	See Table S4	N/A
Recombinant DNA		
pGEM-T-Easy	Promega	Cat#A1360
pTc2KO-bsd, -hyg and -neo	Provided by Fragoso lab, from Fiocruz Paraná	(Pavani et al., 2016)
pnEA/3CH-tcDAC2	This paper	(Diebold et al., 2011; Vincentelli and Romier, 2016)
pX330 plasmid	Genscript	(Peng and Tarleton, 2015)
ptcDAC2	This paper	N/A
Software and algorithms		
EMBOSS-Needle	EMBL-EBI, EMBOSS-Needle	(Madeira et al., 2019)
FlowJo Ver. 10.1r7.	BD Bioscience, FlowJo	N/A
Eukaryotic Pathogen CRISPR guide RNA/ DNA Design Tool	http://gma.ctegd.uga.edu/	(Peng and Tarleton, 2015)
MAFFT	EMBL-EBI, MAFFT	(Kato et al., 2019)
OriginPro Ver. 9.0.0.	OriginLab	N/A
XDS BUILT = 20200131	XDS	(Kabsch, 2010)
Phenix Ver. 1.19rc4_4035	PHENIX	(McCoy et al., 2007; Liebschner et al., 2019)
Coot	Coot	(Emsley et al., 2010)
MolProbity	MolProbity	(Williams et al., 2018)
GraphPad Prism Ver. 7.05.	GraphPad	N/A
Harmony Software Ver. 4.8.	PerkinElmer, Harmony High-Content Imaging and Analysis Software	N/A
Living Image Software Ver. 4.3.	PerkinElmer, Living Image Software	N/A
UCSF Chimera Ver. 1.15.	UCSF Chimera	(Pettersen et al., 2004)
Esript 3	Esript	(Robert and Gouet, 2014)

RESOURCE AVAILABILITY

Lead contact

Further information and requests for resources and reagents should be directed to and will be fulfilled by the lead contact, Christophe Romier (romier@igbmc.fr).

Materials availability

All unique/stable reagents generated in this study will be made available upon request but may require a complete Materials Transfer Agreement if there is potential for commercial applications. The TB compounds are available upon request but can also be synthesized using the protocol provided in this manuscript.

Data and code availability

The crystallographic structures reported in this manuscript have been deposited at the PDB and are publicly available from the date of publication (PDB: 7Q1B, 7Q1C). Accession numbers are listed in the key resource table. Data reported in this manuscript

will be shared by the lead contact upon request. This manuscript does not report original code. Any additional information required to reanalyse the data reported in this paper is available from the lead contact upon request.

EXPERIMENTAL MODEL AND SUBJECT DETAILS

In vivo animal studies

For the *in vivo* infection assays, all animal procedures were approved by the Animal Care and Testing Committee of the Tuiuti University of Paraná (CEUA-UTP No. 006-18) and follow the current ethical regulations. All mice were housed in a pathogen-free animal care facility at Fiocruz Paraná and were kept under controlled environmental parameters of temperature, humidity and positive pressure. Female 5-week-old isogenic BALB/c mice housed 5/cage were used for experiments and grouped in the same cage according to each treatment. The pharmacokinetic study was performed at the CRO Adlego Biomedical (Uppsala, Sweden) with ethics approval granted by the regional animal experimental ethics committee in Stockholm, Sweden. The male NMRI mice were 7-8 weeks at arrival to Adlego's test facility and were acclimatized for a minimum 5 days prior to the study under controlled environmental parameters of temperature and humidity. There were 4 mice in each individually ventilated cage.

Cell lines and microbe strains

Vero cells were cultured in DMEM low glucose medium supplemented with 10% FBS, 10 units/mL of penicillin and 10 μ g/mL of streptomycin. Mouse L929 fibroblasts were cultured in RPMI-1640 medium, containing 10% FBS and 2 mM glutamine. Both cell lines were maintained at 37°C in a humid 5% CO₂ environment and passed every 3-4 days.

T. cruzi Dm28c (Contreras et al., 1988) epimastigotes were cultured in liver infusion tryptose (LIT) medium (Camargo, 1964) supplemented with 10% fetal bovine serum (FBS) without agitation at 28°C. Infective trypomastigote cells of *T. cruzi* Dm28c were obtained by *in vitro* differentiation of epimastigotes (Bonaldo et al., 1988) followed by infection of Vero cells cultured in supplemented DMEM low glucose medium at 37°C in a humid 5% CO₂ environment. After 96 h, infective trypomastigote cells released in the medium were collected by centrifugation and stored under liquid nitrogen.

Infective trypomastigote forms from *T. Cruzi* Tulahuen strain were obtained by *in vitro* infection of mouse L929 fibroblast monolayers cultured in RPMI-1640 medium containing 10% FBS and 2 mM glutamine at 37°C in a humid 5% CO₂ environment (Romanha et al., 2010).

Organisms

The tcDAC2 protein was produced in the *Escherichia coli* BL21(DE3) bacterial strain. More information is provided on the growth conditions in the Methods details section.

METHOD DETAILS

Sequence comparisons

For sequence comparisons, only the deacetylase domains were considered. Those of human HDACs were chosen based on available structural data. For those of trypanosome HDACs, the boundaries of these domains were defined based on inter-parasitic sequence conservation, sequence conservation between the parasitic and human HDACs, secondary structure predictions and disorder predictions. These analyses revealed the existence of a large, almost 200 residues long and potentially disordered region in the center of the trypanosome DAC3 enzymes. Sequence similarities and identities were calculated on the identified deacetylase domains (excluding the DAC3 insertion) using the global EMBOSS-Needle alignment program. Multiple sequence alignments were done with MAFFT and displayed using Esript.

Gene targeted deletion by homologous recombination

Gene targeted deletion was achieved by homologous recombination. The flanking sequences of the tcDAC1 and tcDAC2 genes were initially amplified by PCR from *T. cruzi* Dm28c genomic DNA, using specific primers. Neomycin phosphotransferase or hygromycin phosphotransferase B containing cassettes were amplified from pTc2KO-neo and pTc2KO-hyg (Pavani et al., 2016), respectively. Complete knockout cassettes were obtained by fusion PCR using the individual fragments and external primers.

Single and double knock out strains for both tcDAC1 and tcDAC2 were obtained as previously described (de Souza et al., 2010). Briefly, epimastigote forms of *T. cruzi* Dm28c were transfected with 20 μ g of 5'flank-hyg-3'flank cassette DNA and selected in LIT medium supplemented with hygromycin B (500 μ g/ml). The hygromycin resistant population was subsequently transfected with 20 μ g of 5'flank-neo-3'flank cassette DNA and selected in LIT medium supplemented with hygromycin B (500 μ g/ml) and G418 (500 μ g/ml). The selected population was used for further analyses.

Gene targeted deletion mediated by CRISPR-Cas9

Null mutants were also obtained by the CRISPR/Cas9 methodology using a *T. cruzi* Cas9-GFP expressing strain (Romagnoli et al., 2018). For this purpose, sgRNA sequences were designed using the Eukaryotic Pathogen CRISPR guide RNA/DNA Design Tool (Peng and Tarleton, 2015). DNA templates were generated by using PCR to amplify the sgRNA scaffold sequence from plasmid

pX330 (Peng and Tarleton, 2015) with specific forward primers that contain the T7 promoter and a 20-bp target-specific sequence (Figure S8). The sgRNA was obtained by *in vitro* transcription using the MEGAshortscript T7 kit according to the manufacturer's instructions.

CRISPR-Cas9 mediated knock out was obtained by transfection of 5×10^6 Cas9-GFP expressing cells with 20 μg of specific sgRNA using the U-033 program in an Amaxa Nucleofector device as previously described (Romagnoli et al., 2018). All the analyses were carried out between 1- and 3-days post-transfection.

tcDAC2 complementation assays

A genetic complementation strategy was designed to investigate specific mutations of tcDAC2 which are relevant for the functional characterization of this enzyme. The experimental strategy is based on the CRISPR-Cas9 technology combined with two variants of the tcDAC2 gene sequences, one sensitive and another resistant to a specific sgRNA. The sensitive variant (tcDAC2_sens) serves as a negative control (knock out phenotype) since it has no alteration in the original tcDAC2 sequence (Figure S8A), being cleaved by Cas9 at the same time as the genomic tcDAC2 copy, while the resistant versions contain silent mutations at the sgRNA recognition site, so that the sequence is not cleaved by Cas9 as it is not recognized by the sgRNA (Figure S8B).

Thus, DNA templates designed to be resistant to Cas9 cleavage allow gene replacement by specific mutants of the tcDAC2 gene to test for complementation of genomic knockout (tcDAC2_res, tcDAC2_Y371F, tcDAC2_ΔIns2 and tcDAC2_ΔC). Briefly, tcDAC2_res corresponds to the positive control of the complementation assay, since it contains no change outside the sgRNA recognition site. In contrast, tcDAC2_Y371F, tcDAC2_ΔC and tcDAC2_ΔIns2 are the test molecules, since they contain, respectively, a substitution of the catalytic residue, a deletion of the acidic-rich C terminus, and deletions of an internal loop and of the acidic-rich C terminus.

All five different DNA templates were obtained by site-directed mutagenesis followed by fusion PCR and cloning of the resulting PCR products into pGEM-T-Easy. In addition, a blasticidin S resistance cassette digested from pTc2KO-bsd (derived from pTc2KO-hyg; Pavani et al., 2016) was cloned into all plasmids and the complete constructs were confirmed by DNA sequencing.

Cas9-expressing *T. cruzi* cells were independently transfected with 30 μg of each construct (ptcDAC2_res, ptcDAC2_Y371F, ptcDAC2_ΔIns2, ptcDAC2_ΔC and ptcDAC2_sens; Figure S8C) and the five resulting populations were stably maintained under selection marker pressure (12.5 $\mu\text{g}/\text{ml}$ blasticidin) (Figure S8C). For the complementation assays, the blasticidin-selected populations were transfected with a tcDAC2 specific sgRNA to knockout the endogenous tcDAC2 gene (Figure S8C). All the analyses were performed between 1- and 10-days post-transfection.

Cell cycle analysis

Cell cycle analyses were performed in a FACSAria II (Becton Dickinson) cytometer. A total of 1×10^6 cells was harvested (3000 \times g, 5 minutes), suspended in 100 μL of PBS and mixed with 100 μL of propidium iodide staining solution (3.4 mM Tris-HCl pH 7.4, 0.1% NP40, 10 $\mu\text{g}/\text{ml}$ RNase A, 10 mM NaCl, 30 $\mu\text{g}/\text{ml}$ propidium iodide). Propidium iodide was excited by a 488 nm laser and emitted light was recorded using a 616/23 bandpass filter (PE-Texas Red channel). At least 10,000 single cell events were collected and then gated based on pulse area versus pulse width of the PE-Texas Red channel, excluding cell aggregates and debris. DNA content of gated cell population was analyzed (Nunez, 2001) using FlowJo V10.1r7.

Morphological characterization

Morphological characterization was obtained as previous described (Romagnoli et al., 2018). Specifically, a total of $1-10 \times 10^5$ cells was deposited on a glass slide, allowed to dry and fixed in methanol. After drying, samples were clarified for 4 min with 5 M HCl and washed 5 times with water. After a second drying step, the samples were stained with Panotico. Parasites were observed by light microscopy using a Nikon Eclipse E600 or a Leica DMI8 microscope.

Cell proliferation analysis

For cell proliferation analysis, epimastigote cultures were established at a density of $0.5 - 1 \times 10^6$ cells/ml and population growth was monitored during four days by cell counting in a Z series Coulter counter (Beckman Coulter).

Molecular cloning and mutagenesis

The tcDAC2 wild-type gene and its mutants were PCR-amplified and cloned between the *Nde*I and BamHI restriction sites of the pNEA/3CH vector that encodes a C-terminal His-tag preceded by a protease 3C site (Diebold et al., 2011; Vincentelli and Romier, 2016). *E. coli* DH5 α cells were used for cloning and re-amplification of plasmid vectors, whereas *E. coli* BL21(DE3) cells were used for recombinant production of tcDAC2. The tcDAC2 gene mutants were generated by fusion PCR or rolling circle strategies, gel-purified and ligated into the plasmid pNEA/3CH. All clones were verified by DNA sequencing.

Large-scale production of tcDAC2

E. coli BL21(DE3) cells were transformed with the plasmid coding for the various tcDAC2 constructs of interest using 100 $\mu\text{g}/\text{ml}$ ampicillin for plasmid selection. Ampicillin-resistant colonies were inoculated in large agar plates (15 cm) which were then incubated overnight at 37°C. Film-forming *E. coli* cells were suspended in 10 mL 2xLB medium per large agar plate (15 cm). The bacterial suspension was used to inoculate 5-L Erlenmeyer flasks (1 L 2xLB medium, ampicillin 100 $\mu\text{g}/\text{ml}$) where cells grew (200 rpm, 37°C, and 6 h) until

reaching OD₆₀₀ of 0.8. Induction was done at 22°C by adding 0.7 mM isopropyl-1-thio-β-D-galactopyranoside (IPTG). Harvested bacteria were suspended in lysis buffer (50 mM KCl, 10 mM Tris-HCl pH 8.0) and lysed by sonication. The lysate was clarified by centrifugation (17,000 rpm, 55 min, 4°C, Sorvall Lynx 6000 Thermo Scientific). The supernatant was loaded onto Talon Superflow Metal Affinity Resin pre-equilibrated with the lysis buffer. The His-tagged proteins were released from the Talon resin by protease 3C (home-made) treatment and subsequently loaded onto a 16/60 Superdex 200 gel filtration column pre-equilibrated with the lysis buffer supplemented with 0.5 mM TCEP (pH 7.0).

TB compounds synthesis

All solvents were analytically pure and dried before use. Thin-layer chromatography (TLC) was carried out on aluminum sheets coated with silica gel 60 F254. For column chromatography under atmospheric pressure, silica gel 60 (0.036–0.200 mm) was used. Medium-pressure liquid chromatography was used for more thorough purification of compounds that after gravity column chromatography had purities of < 95%. As stationary phase, silica gel 60 (0.040–0.063 mm) was used. Filling of the columns was performed with the aid of a Cartriger C-670. The elution solvent was mixed and pumped through the column via two pumps (both Pump Module C-601) and the Pump Manager C615. Fractions were collected by a Fraction Collector C-660. All equipment mentioned above was acquired from the manufacturer Büchi. The eluent was also CHCl₃ with 0.25% formic acid and a MeOH gradient. For detection of the product a C-630 UV Monitor was used as well as TLC.

Final compounds were confirmed to be of > 95% purity based on HPLC. Purity was measured by UV absorbance at 254 nm. HPLC instrumentation consisted of an XTerra RP18 column (3.5 mm 3.9x100 mm; Waters, Milford, MA, USA) two LC-10AD pumps, an SPD-M10A VP PDA detector, and an SIL-HT auto sampler all from the manufacturer Shimadzu (Kyoto, Japan). The mobile phase was in all cases a gradient of MeOH/H₂O (starting at 95% H₂O going to 5% H₂O).

Mass spectrometry analyses were performed with a Finnigan MAT 710C (Thermo Separation Products, San Jose, CA, USA) for ESI-MS spectra, and with a LTQ (linear ion trap)-Orbitrap XL hybrid mass spectrometer (Thermo Fisher Scientific, Bremen, Germany) for HRMS-ESI (high-resolution mass spectrometry) spectra. For HRMS analyses, the signal for the isotopes with the highest prevalence was given and calculated for ³⁵Cl and ⁷⁹Br.

¹H and ¹³C NMR spectra were taken on a Varian Gemini 2000 and a Varian Inova 500 using CDCl₃ and DMSO-d₆ as solvents. Chemical shifts (δ, ppm) are referenced to the residual solvent signals.

The general procedure for the synthesis of the cinnamic acid derivatives 2a-e is represented in [Figure S9](#) and described below:

To the respective aldehyde 1a-e (1 eq) and malonic acid (1.2 eq) in pyridine was added piperidine (0.1 eq) and the mixture was stirred at 80°C until completion of reaction was confirmed by TLC. After that, ice and concentrated hydrochloric acid were added. The formed precipitate was collected by filtration, washed with water and dried under reduced pressure to afford the corresponding carboxylic acid 2a-e.

General procedure for conversion of the carboxylic acid into the corresponding hydroxamic acid derivatives 4a-e: PyBOP (1.2 eq) was added to a solution of carboxylic acid 2a-e (1.0 eq) and DIPEA (2.5 eq) in dry THF and the reaction mixture was stirred at RT. After 15 min H₂NOTHP (1.5 eq) was added and the resulting mixture was stirred at RT overnight. The mixture was concentrated and the residue was taken up in DCM and washed with 5% aqueous NaHCO₃. The organic layer was separated, dried over MgSO₄, filtered and evaporated. The crude residue was purified by column chromatography on silica gel (eluent: CHCl₃ with 0.25% Et₃N / MeOH). The THP-protected intermediate 3a-e was dissolved in MeOH and a catalytic amount of 1M aqueous HCl was added. The reaction mixture was stirred at RT until completion of reaction was observed by TLC. The solvent was evaporated and the crude product was purified by column chromatography on silica gel (eluent: CHCl₃ with 0.25% HCOOH / MeOH) to obtain the hydroxamic acid 4a-e.

(2E)-3-(dibenzo[b,d]furan-4-yl)-N-hydroxyprop-2-enamide (4a, TB56): pale pink powder; yield: 26%; ¹H NMR (400 MHz, DMSO-d₆) δ 10.97 (s, 1H, NHOH), 9.11 (s, 1H, NHOH), 8.22 – 8.16 (m, 2H), 7.81 – 7.70 (m, 3H), 7.59 (ddd, J = 8.4, 7.4, 1.3 Hz, 1H), 7.45 (dd, J = 10.8, 4.3 Hz, 2H), 7.02 (d, J = 15.9 Hz, 1H, H_α); ¹³C NMR (101 MHz, DMSO-d₆) δ 162.71 (s), 155.35 (s), 153.26 (s), 132.60 (s), 127.95 (s), 127.67 (s), 124.24 (s), 123.50 (d, J = 6.4 Hz), 123.12 (s), 122.35 (s), 122.03 (s), 121.35 (s), 119.75 (s), 111.68 (s); MS (ESI-, MeOH) *m/z* (%): 252.34 (100) [M-H]⁻; HRMS-ESI *m/z* [M+H]⁺ calcd for C₁₅H₁₂NO₃⁺: 254.0817, found: 254.0809. Purity is higher than 95% as assessed by HPLC.

(2E)-N-hydroxy-3-(naphthalen-2-yl)prop-2-enamide (4b, TB75): off-white powder; yield: 62%; ¹H NMR (400 MHz, DMSO-d₆) δ 10.80 (s, 1H, NHOH), 9.07 (s, 1H, NHOH), 8.07 (s, 1H, H₁), 7.97 – 7.89 (m, 3H, H₅, H₆, H₈), 7.71 (d, J = 8.7 Hz, 1H, H₃), 7.62 (d, J = 15.8 Hz, 1H, H_β), 7.54 (m, J = 6.3, 3.1 Hz, 2H, H₄, H₇), 6.60 (d, J = 15.8 Hz, 1H, H_α); MS (ESI-, MeOH) *m/z* (%): 212.28 (100) [M-H]⁻; HRMS-ESI *m/z* [M+H]⁺ calcd for C₁₃H₁₂NO₂⁺: 214.0868, found: 214.0864. Purity is higher than 95% as assessed by HPLC.

(2E)-3-(2,4-dichlorophenyl)-N-hydroxyprop-2-enamide (4d, TB51): pale yellow powder; yield: 48%; ¹H NMR (400 MHz, DMSO-d₆) δ 10.88 (s, 1H, NHOH), 9.16 (s, 1H, NHOH), 7.72 (d, J = 8.8 Hz, 1H, H₆), 7.70 (d, J = 2.1 Hz, 1H, H₃), 7.67 (d, J = 15.9 Hz, 1H, H_β), 7.48 (dd, J = 8.4, 1.8 Hz, 1H, H₅), 6.53 (d, J = 15.7 Hz, 1H, H_α); MS (ESI-, MeOH) *m/z* (%): 230.17 (100) [M-H]⁻; HRMS-ESI *m/z* [M+H]⁺ calcd for C₉H₈Cl₂NO₂⁺: 231.9932, found: 231.9928. Purity is higher than 95% as assessed by HPLC.

(2E)-N-hydroxy-3-(3-phenoxyphenyl)prop-2-enamide (4e, TB72): off-white powder; yield: 39%; ¹H NMR (400 MHz, DMSO-d₆) δ 10.72 (s, 1H, NHOH), 9.05 (s, 1H, NHOH), 7.47 – 7.36 (m, 4H, H_β, H_{3'}, H_{4'}, H_{5'}), 7.33 (d, J = 7.7 Hz, 1H, H₆), 7.22 – 7.13 (m, 2H, H₂, H₅), 7.04 (dd, J = 8.6, 0.9 Hz, 2H, H_{2'}, H_{6'}), 7.00 (dd, J = 8.0, 1.8 Hz, 1H, H₄), 6.43 (d, J = 15.8 Hz, 1H, H_α); MS (ESI-, MeOH) *m/z* (%): 254.30 (100) [M-H]⁻; HRMS-ESI *m/z* [M+H]⁺ calcd for C₁₅H₁₄NO₃⁺: 256.0974, found: 256.0969. Purity is higher than 95% as assessed by HPLC.

tcDAC2 activity and inhibition assays

Upon initial purification of the tcDAC2 enzyme, several assays were investigated to measure tcDAC2 activity. Two assays have been shown to measure reproducibly tcDAC2 deacetylase activity and have been used subsequently for our mutational and inhibition studies. First, tcDAC2 activity tests were carried out with the Ac-Leu-Gly-(TFA)Lys-AMC substrate, according to the manufacturer's instructions with a substrate concentration of 50 μ M. Fluorescence was measured in a plate reader (BMG Polarstar) with excitation at $\lambda = 390$ nm and emission at $\lambda = 460$ nm. IC₅₀ values were determined with OriginPro (version 9.0.0, Northampton, Massachusetts). Second, tcDAC2 activity tests were carried out with the fluorogenic substrate ZMTFAL (Z-(F3Ac)Lys-AMC) (Heltweg et al., 2004) in 1/2 AreaPlate-96 F microplates (PerkinElmer). The total assay volume of 30 μ L contains 12.5 μ L assay buffer (15 mM Tris, pH 7.5, 50 mM KH₂PO₄, 3 mM MgSO₄·7 H₂O and 10 mM KCl), 10 μ L of enzyme solution in assay buffer, 2.5 μ L of increasing concentrations of inhibitors in DMSO and 5 μ L of the fluorogenic substrate ZMTFAL (Z-(F3Ac)Lys-AMC) in assay buffer (25 μ M). After incubation (90 min, 37°C) 30 μ L of stop solution, containing 2.5 μ L Trichostatin A (TSA) (33 μ M) and 5 μ L trypsin (6 mg/mL) in trypsin buffer (50 mM Tris-HCl, pH 8.0, 100 mM NaCl), were added. After incubation (30 min, 37°C), the fluorescence signal ($\lambda_{\text{ex}} = 390$ nm, $\lambda_{\text{em}} = 460$ nm) was measured on a BMG LABTECH POLARstar OPTIMA plate reader (BMG Labtechnologies, Germany).

hsHDAC1/6 activity and inhibition assays

Commercially available human recombinant HDAC1 and human recombinant HDAC6 were used. Activity assays were performed as described before (Heltweg et al., 2005). Total amount of assay volume (60 μ L), containing 52 μ L of enzyme solution in incubation buffer (50 mM Tris-HCl, pH 8.0, 137 mM NaCl, 2.7 mM KCl, 1 mM MgCl₂, and 1 mg/mL bovine serum albumin), 3 μ L of increasing concentrations of inhibitors in DMSO and 5 μ L of the fluorogenic substrate ZMAL (Z-(Ac)Lys-AMC, 126 μ M), were pipetted into OptiPlate™-96 F black microplates (PerkinElmer). Followed by an incubation step (90 min, 37°C). Stop solution (60 μ L), containing 5 μ L Trichostatin A (TSA, 33 μ M) and 10 μ L trypsin (6 mg/mL) in trypsin buffer (Tris-HCl 50 mM, pH 8.0, NaCl 100 mM), were added. After incubation (30 min, 37°C) the fluorescence signal ($\lambda_{\text{ex}} = 390$ nm, $\lambda_{\text{em}} = 460$ nm) was measured on a BMG LABTECH POLARstar OPTIMA plate reader (BMG Labtechnologies, Germany).

hsHDAC8 activity and inhibition assays

For HDAC8 activity testing the commercially available Fluor-de-Lys (FDL) drug discovery kit was used. The assay was performed according to the manufacturer's instructions. Enzyme solution (15 μ L), inhibitor in increasing concentrations (10 μ L) and FDL substrate solution (25 μ L) were pipetted into 1/2 AreaPlate-96 F microplates (PerkinElmer) and the assay was incubated for 90 min at 37°C. Developer solution (50 μ L) was added. After incubation (45 min, 30°C) the fluorescence signal ($\lambda_{\text{ex}} = 390$ nm, $\lambda_{\text{em}} = 460$ nm) was measured on a BMG LABTECH POLARstar OPTIMA plate reader (BMG Labtechnologies, Germany).

Dynamic light scattering

The dynamic light scattering (DLS) experiments were conducted with tcDAC2 protein solutions (2mg/ml) in a buffer containing 50 mM KCl, 10 mM Tris-HCl (pH = 8.0) and 0.5 mM TCEP using a DynaPro NanoStar instrument (Wyatt). Protein solutions were centrifuged at 13,000 rpm for 10 min prior to DLS measurement in order to remove impurities. Before measurement the temperature was equilibrated to 20°C.

Differential scanning fluorimetry

Thermal stability of tcDAC2 was measured by a label-free differential scanning fluorimetry (DSF) approach using a Prometheus NT.48 instrument (NanoTemper Technologies). Specifically, the shift of intrinsic tryptophan fluorescence of tcDAC2 proteins upon gradual temperature-triggered unfolding (temperature gradient 20°C to 95°C) was monitored by detecting the emission fluorescence at 330 and 350 nm. The measurements were carried out in nanoDSF-grade high sensitivity glass capillaries (NanoTemper Technologies) at a heating rate of 1°C/min. Protein melting points (T_m) were inferred from the first derivative of the ratio of tryptophan emission intensities at 330 and 350 nm. All the assays were done in triplicate.

Limited proteolysis assay

Limited proteolysis reactions contained 20 μ L reaction buffer (50 mM KCl, 10 mM Tris-HCl pH 8.0), 7 μ L protein (6.5 mg/ml) and 3 μ L serially diluted trypsin protease (0.1 to 0.000001 mg/ml). The reactions were incubated at 4°C for 1 h, and then stopped by addition of 15 μ L Laemmli buffer. Limited proteolysis products were analyzed by SDS-PAGE and visualized by Coomassie Brilliant Blue staining.

Protein crystallization experiments and data collection

The tcDAC2 enzyme in complex with Quisinostat (QSN) or TB56 inhibitors was prepared for crystallization by mixing the purified protein (concentration of 0.12 mM to 0.3 mM) with a three or five-fold molar excess of the inhibitors and incubated for 1 h at 4°C. Crystallizations were performed in 96-, 48- or 24-well plates (MRC). Crystals of the tcDAC2/QSN complex were obtained in 5% PEG 6000 and 0.1 M HEPES pH 7.0 or pH 7.5. Crystals of the tcDAC2/TB56 complex were obtained in 8% PEG8000, 0.2 M MgCl₂, and 0.1 M Bis-tris or Bis-tris propane pH 6.5. Crystals used for X-ray data collection were briefly transferred into reservoir solution supplemented with 22% glycerol or PEG200 and flash-frozen in liquid nitrogen. Crystallographic data were collected at 100 K on Swiss Light Source (SLS) synchrotron beamline PX-III and SOLEIL synchrotron beamline PROXIMA2.

Structure determination and refinement

Crystallographic data were processed and scaled using XDS (Kabsch, 2010). The structure of tcDAC2/QSN complex at 1.7 Å resolution was solved by molecular replacement with Phaser (McCoy et al., 2007) implemented in Phenix (Liebschner et al., 2019) using our tcDAC2 homology-derived model as a search model. The structure of the tcDAC2/TB56 complex at 2.3 Å resolution was solved by molecular replacement with Phaser (McCoy et al., 2007) implemented in Phenix (Liebschner et al., 2019) using the tcDAC2/QSN structure. The initial models were refined through several cycles of manual building using Coot (Emsley et al., 2010) and automated refinement with Phenix (Liebschner et al., 2019). The final models were validated using tools provided in Coot (Emsley et al., 2010) and Molprobity (Williams et al., 2018). Video animations were produced with Chimera (Pettersen et al., 2004).

Determination of cytotoxicity on L929 cells

To assess the cytotoxicity over L929 cells, 4,000 L929 cells suspended in 200 μL of RPMI-1640 medium plus 10% FBS and 2 mM glutamine were added to each well of a 96-well microtiter plate and were incubated for three days at 37°C in a humid 5% CO₂ environment. The medium was then replaced, and the cells were exposed to compounds at eight different concentrations. After up to 72 h of incubation with the compounds, alamarBlue™ was added, incubated for 4–6 h, and the absorbance at 570 and 600 nm was assessed. Controls including untreated and 1% DMSO-treated cells were run in parallel. Four technical replicates were run in the same plate and the experiments were repeated at least in two biological replicates. The results were expressed as the percent difference in the reduction between treated (TC) and untreated cells (UT), using the equation: $\frac{((117,216)(Abs_{570} TC) - (80,586)(Abs_{600} TC))}{((117,216)(Abs_{570} UT) - (80,586)(Abs_{600} UT))} \times 100$. Dose-response curves were plotted using GraphPad Prism version 7.05. Non-linear regression was used to determine CC₅₀ values.

L929 cell infection assays

The *in vitro* test of trypanocidal activity was performed as previously described (Romanha et al., 2010; Buckner et al., 1996), using the *T. cruzi* Tulahuen strain expressing the *Escherichia coli* β-galactosidase gene. Specifically, 4,000 L929 cells were added in 80 μL of supplemented medium, without phenol red, to each well of a 96-well microtiter plate. After an overnight incubation, 40,000 trypomastigotes suspended in 20 μL volume were added to the cells and incubated for 2 h. Medium containing parasites that did not penetrate the cells was replaced with 200 μL of fresh medium and incubated for an additional 48 h, allowing the establishment of infection. The medium was then replaced by compounds diluted at different concentrations in fresh medium (200 μL) and the plate was incubated for 96 h at 37°C. After this period, 50 μL of 500 μM chlorophenol red β-D-galactopyranoside in 0.5% Nonidet P40 was added to each well, followed by an incubation of 18 h at 37°C, after which the absorbance at 570 nm was measured. Controls included: uninfected cells, untreated infected cells, infected cells treated with 3.8 μM benznidazole (positive control) or cells exposed to 1% DMSO. The results were expressed as the percentage of *T. cruzi* growth inhibition in compound-tested cells as compared to the infected cells and untreated cells. Quadruplicates were run in the same plate and the experiments were repeated at least in two biological replicates. Compounds and the reference drug benznidazole were serially diluted (1:4 ratio) in RPMI medium, to obtain eight-points (from 80 μM to 0.0025 μM). Dose-response curves were plotted using GraphPad Prism version 7.05. Non-linear regression was used to determine the EC₅₀ values.

Intracellular *T. cruzi* inhibition in infected Vero cells

Vero cells were cultured in DMEM low glucose medium supplemented with 10% FBS, 10 units/mL of penicillin and 10 μg/mL of streptomycin at 37°C in a humid 5% CO₂ environment. Infective trypomastigote cells of *T. cruzi* Dm28c were obtained as previously described (Bonaldo et al., 1988) and stored under liquid nitrogen. Trypomastigotes from a frozen stock were amplified in Vero cells for one passage before starting the assays. For Vero cells infection assays, 3x10³ cells adhering to 96-well plates were infected with 6x10⁴ trypomastigotes in a MOI of 20:1 in four technical replicates for 16 h. After this time, the wells were washed twice with PBS to remove the parasite cells that remained free. TB56, Quisinostat (QSN) and the reference drug benznidazole (BZN) were initially diluted in DMSO to obtain a ten-point serial dilution (1:3 ratio) from 18 mM to 0.905 μM. Subsequently, 1 μL of each dilution was added to 200 μL of culture medium to obtain final culture concentrations from 90 μM to 0.045 μM in 10 points of 1:3 factor each (final DMSO was 0.5% v/v). The medium containing the compounds was homogenized prior to addition to cells. Medium containing 0.5% DMSO (v/v) was administered to control wells of uninfected and untreated cells. Cultures were maintained under the same conditions for 24, 48 and 72 h to determine EC₅₀ and CC₅₀ values. For image analysis, the cells were washed twice with PBS prior to and after fixation with 4% paraformaldehyde (PFA) for 15 min and stained with 0.001% Evans' blue and 1 μg/mL DAPI. Images of 25 fields per well were acquired on an Operetta Image System (PerkinElmer) and analyzed using the Harmony software to discriminate nucleus, cytoplasm and the spots delimited for the intracellular amastigotes. The number of cells and amastigotes per well were determined and dose-response curves were plotted using GraphPad Prism version 7.05. Non-linear regression was calculated to determine CC₅₀ and EC₅₀ for cells and parasites, respectively. The inhibition ratio (in %) was calculated based on the mean of cells or amastigotes from the infected untreated wells.

Pharmacokinetic study

The TB56 pharmacokinetic study was performed using four NMRI mice (Charles River, Germany) where two mice were administered 50 mg/kg TB56 intravenously (i.v.) and two mice were administered 50 mg/kg TB56 orally by gavage (p.o.). The formulation of TB56

was: 5 mg/ml TB56 in 7% DMSO, 35% (w/v) HP β CD in DPBS, pH ca 7. The health status of the mice was followed and blood sampling took place at 15, 60 and 180 min (i.v.) and 30, 60 and 180 min (p.o.). Following the last blood sampling the animals were euthanized. The blood samples were immediately centrifuged and the plasma transferred and frozen. Bioanalysis of the plasma samples was performed by LC-MS/MS using an ACQUITY UPLC-TQD (Waters). Propranolol was used as an internal standard. Preparation of plasma samples: 20 μ l of each plasma sample and the standard samples (prepared from TB56 DMSO stocks using inactive mouse plasma) were added to 100 μ l (5 volumes) cold acetonitrile with 2 μ M propranolol (internal standard) in a 96-well plate. The plate was left for 20 minutes equilibration on a shaker table. The plate was then centrifuged for 15 min at 2800 rpm, 4°C and 50 μ l of the supernatants were transferred to wells containing 100 μ l distilled water in another 96-well plate. The plate was left to equilibrate on a shaker table for 10 minutes. The plate was sealed and the LC-MSMS experiments performed. The analysis of each sample was performed in duplicate. The quantification of the plasma concentrations was done with the eight point calibration curve obtained from the TB56 standard plasma samples ranging from 160 μ M to 9.8 nM ($R^2 = 0.999$).

Mouse infection assays

Mouse infection assays were performed with three groups of five mice each of 5-week old Balb/C females infected by intraperitoneal injection with 2×10^5 *T. cruzi* Dm28c trypomastigotes expressing firefly luciferase (Henriques et al., 2014). One group comprised the untreated controls and a second group was treated with the reference drug benznidazole, while the third group received TB56. TB56 and benznidazole were prepared in 7% DMSO (v/v), 40% (2-Hydroxypropyl)- β -cyclodextrin (v/w) in DPBS. Intraperitoneal injections were performed from day 4 to day 8 post-infection with 50 mg/kg/day of each compound. Mice from the control group were treated with vehicle only. Parasite load was determined by luminescence quantification using D-luciferin administered at 150 mg/kg 10–20 min before data acquisition using a IVIS Spectrum CT (Perkin-Elmer) on dorsal and ventral positions, on days 3, 7 and 9 post infection. Images were processed using the Living Image v.4.3 software. Regions of interest (ROI) were selected to the full body including tail. Background auto luminescence was calculated using the same ROI size where indicated. Total flux [photons/second] was considered for calculations and average radiance [photons/sec/cm²/steradian] for image units. Statistical analysis was performed by using one-way ANOVA with spherical data and Tukey's multiple tests in GraphPad Prism v.7.05.

QUANTIFICATION AND STATISTICAL ANALYSIS

Quantification methodologies and details of specific statistical tests are included under the relevant subsections of the Methods details section. Information regarding the number of mammalian host cells, *T. cruzi* cells, animals, biological and technical replicates is provided in figures, figure legends and in the respective subsections of the Methods details section. In all cases, biological replicates are defined as independent experiments and technical replicates as replicates done in the same experiment.

In vitro HDAC inhibition assays are represented as mean \pm SD of technical triplicates. For *T. cruzi* cell proliferation analysis, the data points represent the average of biological duplicates shown as mean \pm SD. Cell Cycle diagrams represent the distribution of the different stages of the 10,000 single cell analyzed. In L929 and Vero cell toxicity assays and in the respective L929 and Vero cell infection assays with *T. cruzi* Tulahuen and Dm28c strains, the datapoint represent the mean of technical replicates and the error bars represent standard deviation (SD) of the experimental values. CC₅₀ and EC₅₀ for cells and parasites, respectively, were determined by using non-linear regression. Statistical analyses for the *in vivo* data were performed by using one-way ANOVA with spherical data and Tukey's multiple tests in GraphPad Prism.

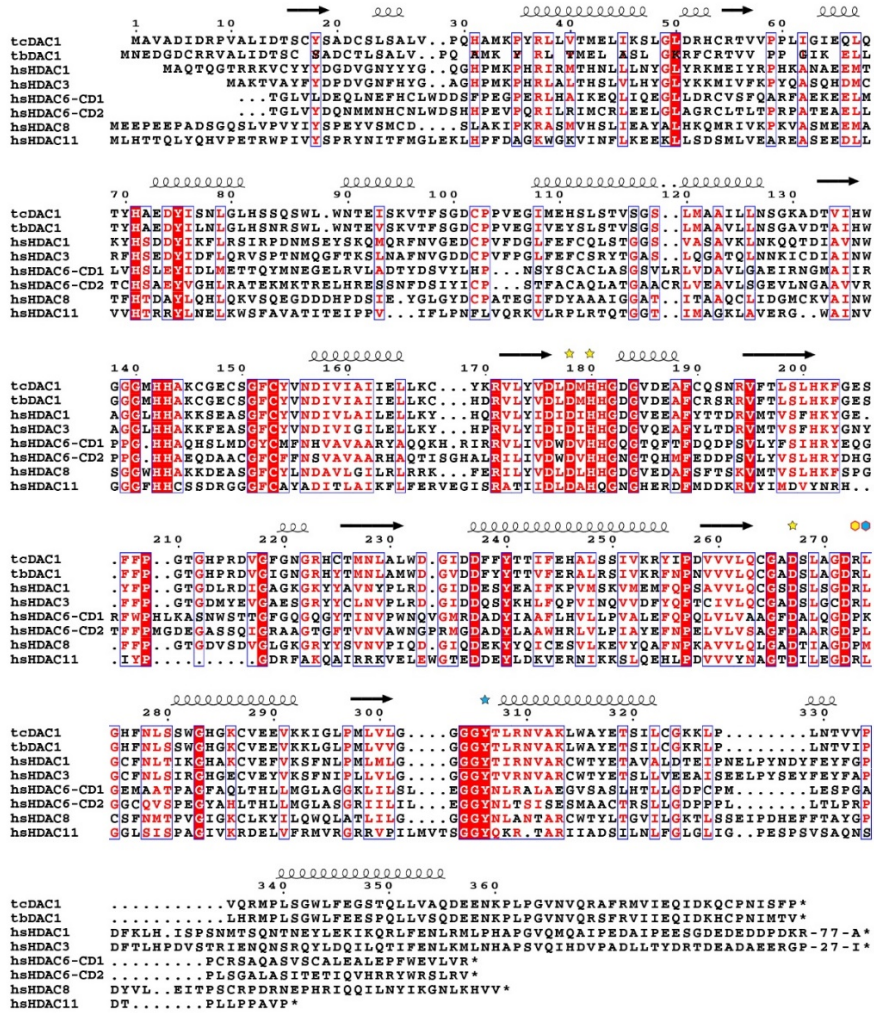
Supplemental information

**Species-selective targeting of pathogens revealed
by the atypical structure and active site
of *Trypanosoma cruzi* histone deacetylase DAC2**

Martin Marek, Elizabeth Ramos-Morales, Gisele F.A. Picchi-Constante, Theresa Bayer, Carina Norström, Daniel Herp, Policarpo A. Sales-Junior, Eloise P. Guerra-Slompo, Kristin Hausmann, Alokta Chakrabarti, Tajith B. Shaik, Annika Merz, Edouard Troesch, Karin Schmidtkunz, Samuel Goldenberg, Raymond J. Pierce, Marina M. Mourão, Manfred Jung, Johan Schultz, Wolfgang Sippl, Nilson I.T. Zanchin, and Christophe Romier

A

DAC 1



B

DAC 2

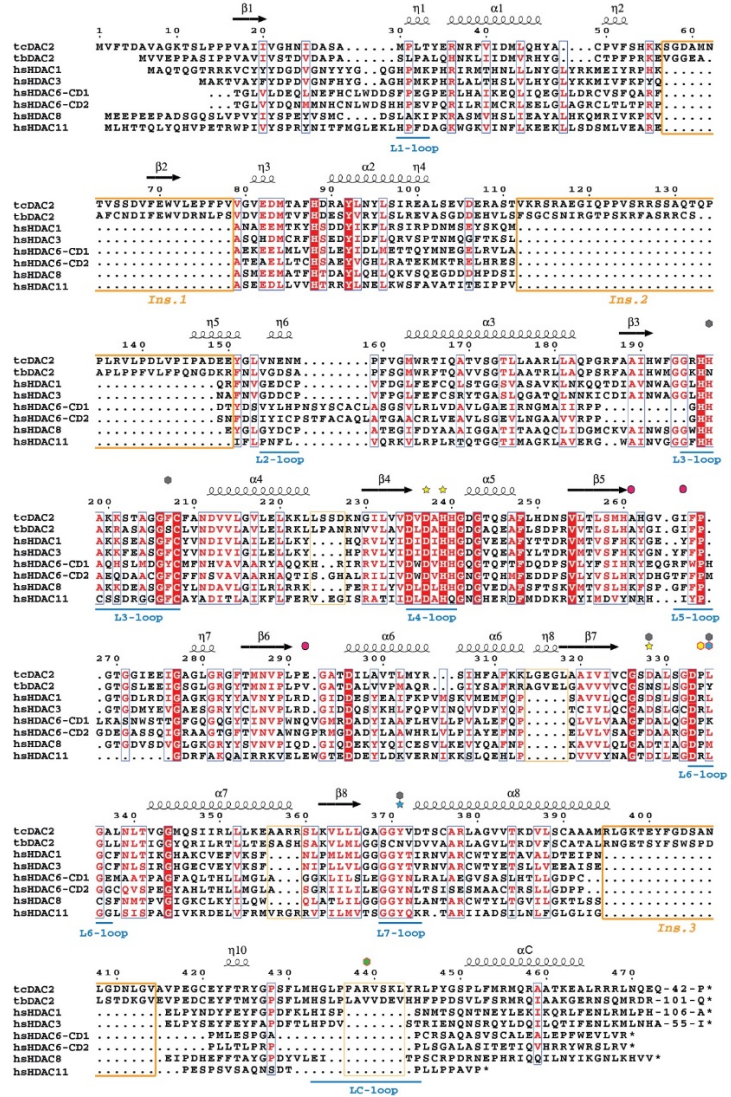


Figure S1. Multiple sequence alignments of the trypanosome class I HDACs. Related to Figure 1. **(A)** Multiple sequence alignment of trypanosome (tc, *Trypanosoma cruzi*; tb, *Trypanosoma brucei*) DAC1 enzymes with class I, class IIb and class IV human (hs) HDACs. Residues involved in zinc binding are shown with yellow stars, the catalytic tyrosine as blue star. The yellow diamond marks the residue in the active site L6 loop distinguishing the HDAC1-3 and HDAC11 isozymes subfamilies from the other human HDAC isozymes. The blue diamond marks the neighboring residue in the L6 loop gatekeeping the HDAC active sites. Secondary structure elements from hsHDAC1 are shown above the alignment. The C-terminal sequences of some HDACs have been removed for clarity and the number of residues removed is indicated. '*' marks the end of the sequences. **(B)** Same as in (A) for DAC2 enzymes. Insertions specific to DAC2 enzymes are boxed and active site loops are indicated. The green diamond marks the arginine that caps tcDAC2 L6 loop. Purple circles mark important residues forming the tcDAC2-unique pocket. Grey diamonds mark non-conserved active site residues in tbDAC2. Secondary structure elements (α , α -helices; β , β -strands; η , 3_{10} -helices) are those observed in tcDAC2 structure. The alignments were produced with Esript (Robert and Gouet, 2014).

Figure S2. Multiple sequence alignments of the trypanosome class IIb HDACs. Related to Figure 1. **(A)** Multiple sequence alignment of trypanosome (*tc*, *Trypanosoma cruzi*; *tb*, *Trypanosoma brucei*) DAC3 enzymes with class IIa and IIb human (*hs*) HDACs. For clarity, the large insertion in the middle of the DAC3 enzymes is only partially shown and the number of residues removed from the alignment is displayed. Residues involved in zinc binding are shown with yellow stars, the catalytic tyrosine as blue star. The yellow diamond marks the residue in the active site L6 loop distinguishing the HDAC1-3 and HDAC11 isozymes subfamilies from the other human HDAC isozymes. The blue diamond marks the neighboring residue in the L6 loop gatekeeping the HDAC active sites. Secondary structure elements are shown above the alignment. The C-terminal sequences of some HDACs have been removed for clarity. '*' marks the end of the sequences. **(B)** Same as in (A) for DAC4 enzymes. The alignments were produced with Esprict (Robert and Gouet, 2014).

A

	hHDAC1	hHDAC2	hHDAC3	hHDAC8	tbDAC1	tcDAC1	tbDAC2	tcDAC2
hHDAC1		92,6	63,0	39,5	39,1	39,1	26,1	25,5
hHDAC2	97,3		61,7	39,7	38,7	36,4	23,7	26,2
hHDAC3	82,0	80,7		39,8	37,7	39,6	26,2	25,2
hHDAC8	60,5	61,0	59,4		33,4	32,3	25,8	25,1
tbDAC1	55,3	55,4	50,4	52,10		85,6	25,4	25,1
tcDAC1	55,1	50,0	54,8	51,10	92,3		27,1	25,0
tbDAC2	41,7	37,1	38,4	41,70	37,2	38,1		51,0
tcDAC2	37,4	40,6	37,7	39,80	33,5	38,9	64,7	

Identities

Similarities

B

	hHDAC4	hHDAC7	hHDAC6CD1	hHDAC6CD2	hHDAC10CD1	tbDAC3	tcDAC3	tbDAC4	tcDAC4
hHDAC4		73,9	37,9	44,7	36,2	30,1	32,9	26,3	25,0
hHDAC7	85,3		36,8	43,0	36,6	32,6	33,0	23,2	28,3
hHDAC6CD1	52,6	51,9		47,0	54,0	30,2	31,8	24,5	26,0
hHDAC6CD2	57,8	54,1	63,9		50,8	32,5	33,9	26,3	28,0
hHDAC10CD1	52,4	51,1	70,9	64,9		33,2	33,3	23,2	28,0
tbDAC3	42,4	44,8	43,5	46,5	45,6		64,0	25,0	26,9
tcDAC3	47,6	46,0	45,0	47,9	47,1	74,5		27,8	26,9
tbDAC4	37,7	31,2	36,1	36,2	31,6	38,1	40,4		63,3
tcDAC4	33,4	38,7	37,8	39,0	39,3	40,7	39,2	74,4	

Identities

Similarities

C

	tbDAC1	tcDAC1	tbDAC2	tcDAC2	tbDAC3	tcDAC3	tbDAC4	tcDAC4
tbDAC1		85,6	25,4	21,5	23,2	24,9	18,7	18,6
tcDAC1	92,3		27,1	25,0	28,0	21,6	16,4	16,8
tbDAC2	37,2	38,1		51,0	18,0	18,6	18,8	21,9
tcDAC2	33,5	38,9	64,7		22,3	19,0	19,2	20,9
tbDAC3	36,0	34,9	28,4	34,3		64,0	25,0	26,9
tcDAC3	35,4	33,6	29,0	30,4	74,5		27,8	26,9
tbDAC4	31,1	27,6	28,9	32,4	38,1	40,4		63,3
tcDAC4	29,4	29,0	32,6	33,4	40,7	39,2	74,4	

Identities

Similarities

< 20%	20-30%	30-40%	40-50%	50-60%	60-70%	70-80%	80-90%	> 90%

Figure S3. Sequence identities/similarities between human and trypanosome HDACs. Related to Figure 1. **(A-C)** Sequence identities (upper right part of the tables) and sequence similarities (lower left part of the tables) between (A) class I human and trypanosome HDACs, (B) class II human and trypanosome HDACs, and (C) trypanosome HDACs. The colour code is provided at the bottom of the figure. Sequence identities/similarities were calculated with the EMBOSS Needle program using only the catalytic domains of each HDAC as defined by structural data. Sequence boundaries of the catalytic domains for the trypanosome HDACs, except for the DAC2 enzymes, were defined based on their multiple sequence alignments. The large additional domain within DAC3 enzymes was removed for sequence identities/similarities calculations.

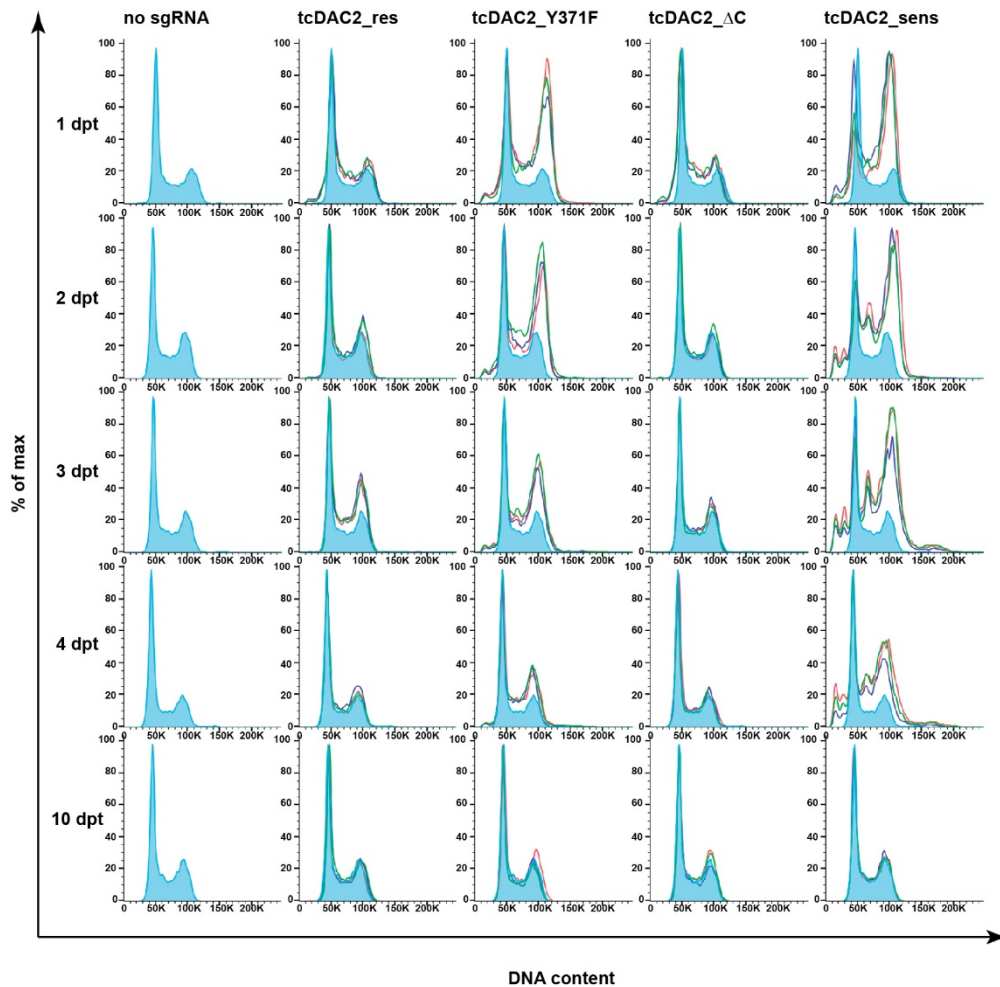


Figure S4. tcDAC2 complementation assay shows lethal phenotype for the Y371F mutation but not for removal of the non-conserved acidic C-terminal tail. Related to Figure 2. The genetic complementation strategy is based on the CRISPR-Cas9 technology combined with two variants of the tcDAC2 gene sequences, one sensitive and another resistant to a specific sgRNA, as described in the STAR Methods section. Cell cycle progression of the cell lines carrying the different genetic variants was analyzed at the indicated times after sgRNA transfection. Cyan curves show wild-type cell profiles. The red, blue and green line curves show mutant cell profiles. The tcDAC2_sens variant is the negative control (knockout phenotype) and the tcDAC2_res variant is the positive control for tcDAC2 complementation. The tcDAC2_Y371F and tcDAC2_ΔC variants contain, respectively, the substitution of the catalytic tyrosine residue by a phenylalanine and a deletion of the glutamic acid-rich C-terminal region. The tcDAC2_Y371F variant shows phenotype similar to the tcDAC2_sens variant which does not complement the deletion of the genomic copy of tcDAC2. dpt – days post-transfection. All assays were performed with biological triplicates. Each cell cycle analysis represents data from at least 10,000 single cells.

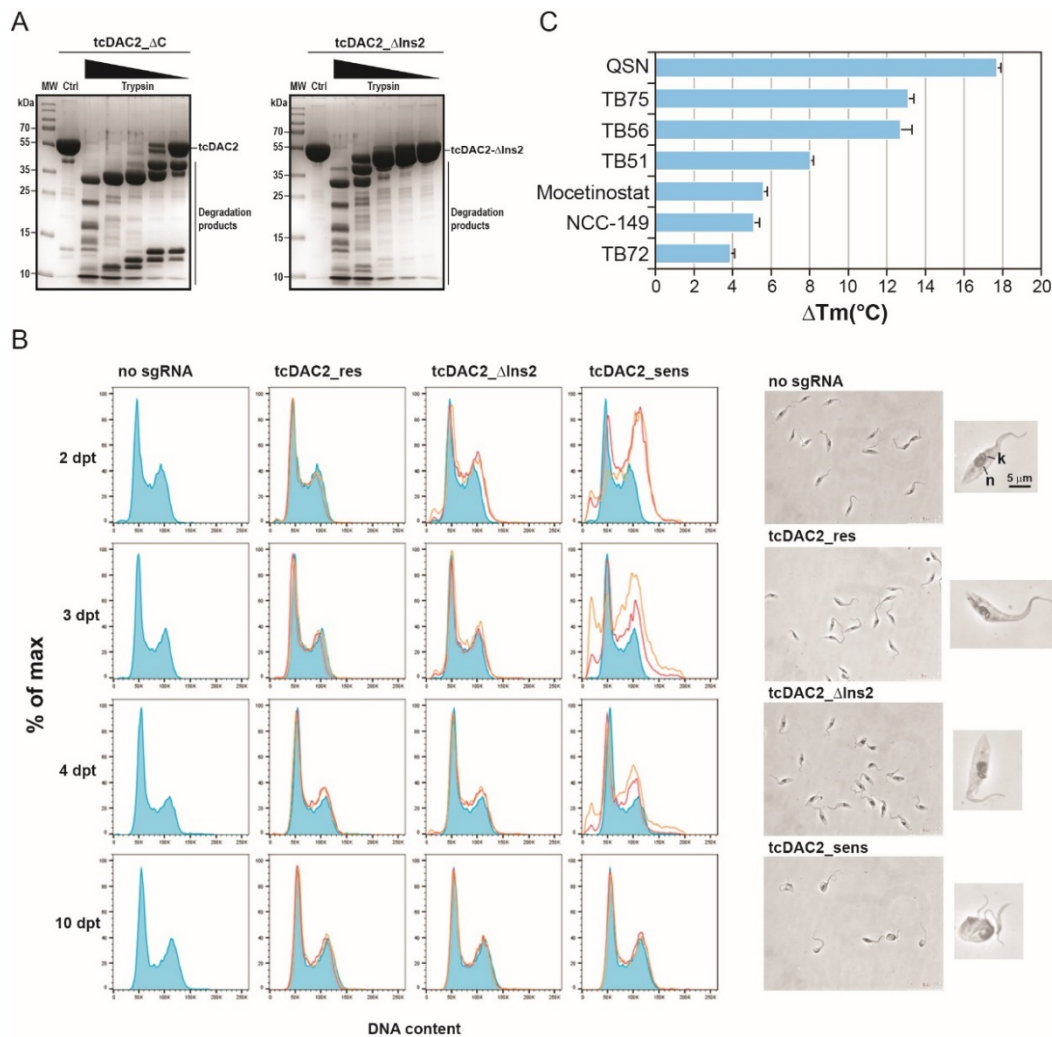


Figure S5. Stabilization of tcDAC2 by protein engineering and inhibitors. Related to Figures 3 and 4. **(A)** Comparative limited proteolysis analysis of tcDAC2_ΔC and tcDAC2_ΔIns2. Removal of a part of Insertion2 in tcDAC2 has a strong protective effect on proteolysis, suggesting that Insertion2 is an accessible surface loop. **(B)** *T. cruzi* complementation assay with tcDAC2_ΔIns2 shows no deleterious effect of this variant. Cell cycle progression (left) and light microscopy images (right) of parasites carrying the different genetic variants were analyzed at the indicated times after sgRNA transfection. Cyan curves show wild-type cell profiles. The red and yellow line curves show mutant cell profiles. tcDAC2_sens: negative control (knockout phenotype); tcDAC2-res: positive control for tcDAC2 complementation; tcDAC2_ΔIns2: loop deletion. The phenotype of cells carrying the tcDAC2_ΔIns2 and tcDAC2_res variants is similar showing that tcDAC2_ΔIns2 can efficiently complement tcDAC2 gene deletion. n – nucleus, k – kinetoplast, dpt – days post-transfection. All assays were performed with biological duplicates. Each cell cycle analysis represents data from at least 10,000 single cells. **(C)** Thermal stability of tcDAC2_ΔIns2 in presence of various inhibitors. The values on the abscissa represent the gain in °C of melting temperature (ΔT_m) of the inhibited enzyme compared to the enzyme alone.

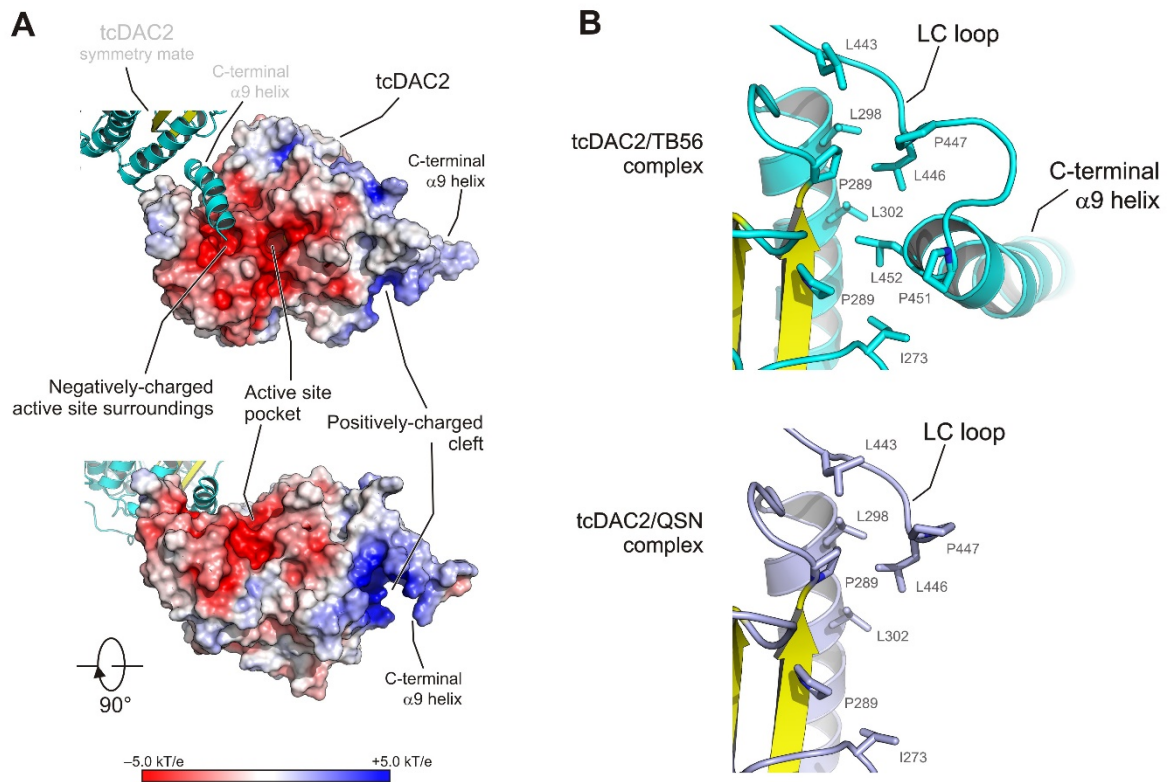


Figure S6. Non-canonical nature of tcDAC2 C-terminal helix ($\alpha 9$). Related to Figure 4. **(A)** Crystallographic contacts made by tcDAC2 $\alpha 9$ C-terminal helix. The electrostatic potential (red, negative potential; blue, positive potential) is displayed at the surface of the crystallographic symmetric tcDAC2 monomer. This shows that both tcDAC2 $\alpha 9$ C-terminal helix and the region of tcDAC2 core, where HDACs normally interact with their C-terminal helices, are both positively charged. This explains that these two regions cannot interact with each other due to repulsive electrostatic contacts. **(B)** Hydrophobic interactions positioning differently the start of tcDAC2 αC -helix. These features are conserved in both structures solved, showing that they cannot be due to the crystal packing observed in the tcDAC2/TB56 structure.

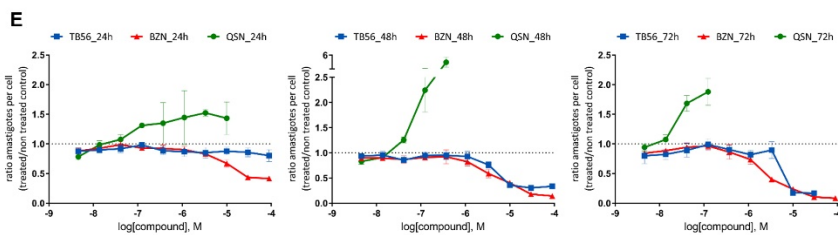
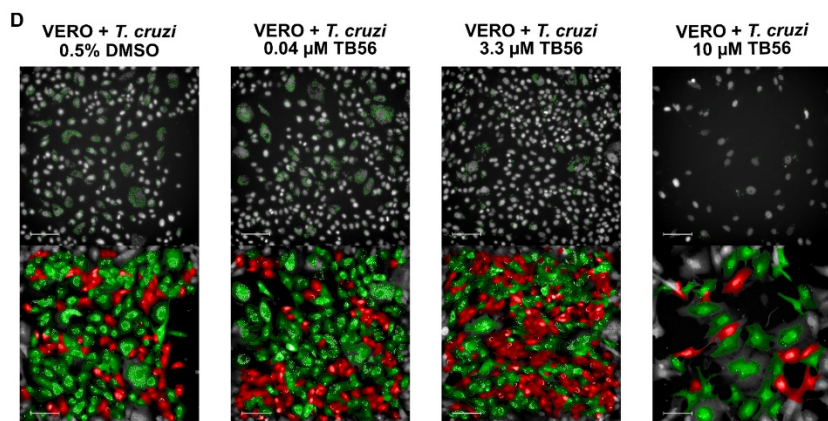
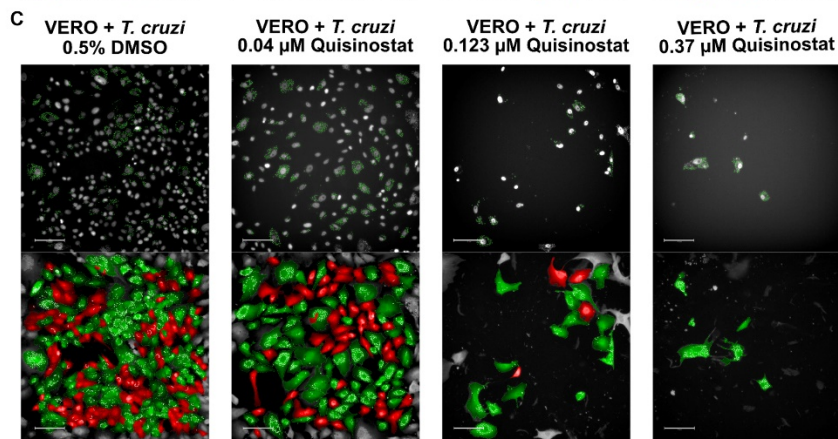
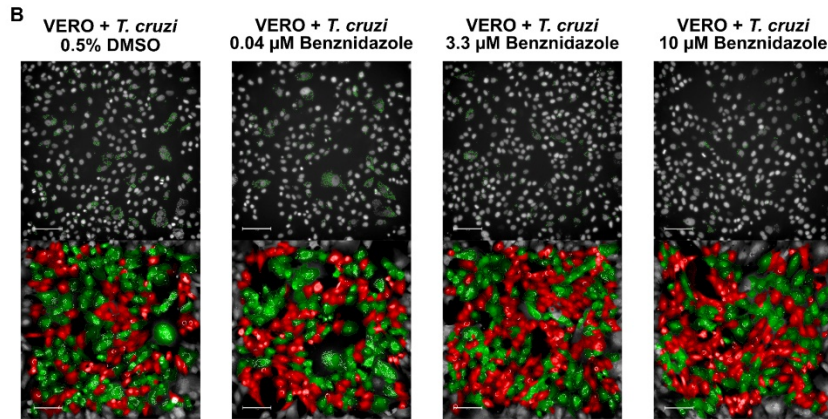
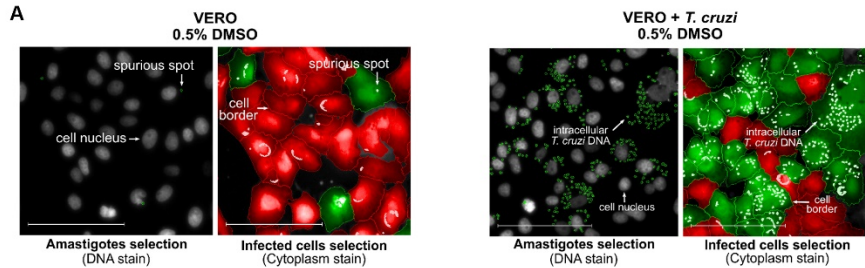


Figure S7. Representative images from high-content image-based experiments for the determination of *T. cruzi* inhibition by Benznidazole (BZN), Quisinostat (QSN) and TB56 in Vero cells infection assays.

Related to Figure 7. **(A)** Representative images of uninfected (left images) and infected (right images) control cells both treated with DMSO showing the relevant features for assay quantification. Nuclei from Vero cells and from intracellular *T. cruzi* amastigotes were visualized by staining the DNA with 1 µg/mL DAPI. The images of the left panels show the DNA-stained nuclei of Vero cells (grey) and *T. cruzi* amastigote spots (green). In the right panels, Vero cells border and *T. cruzi* amastigotes spots were determined using the Harmony software (PerkinElmer). In addition, the images on the right panels show overlays of the DNA-stained images with the images of the cell borders and *T. cruzi* amastigotes spots (white). The non-infected and infected Vero cells are shown in red and green, respectively. Irregularities in nuclei staining of non-infected Vero cells can be misidentified by the software and are labelled as spurious spots. Size bars = 100 µm. **(B)** Images from the assays performed to determine the inhibition effect of BZN on *T. cruzi* amastigotes in infected Vero cells. Sample images from the cells treated with DMSO and 0.04 µM, 3.3 µM and 10 µM of BZN are shown. **(C)** Images from the assays performed to determine the inhibition effect of QSN on *T. cruzi* amastigotes in infected Vero cells. Sample images from the cells treated with DMSO and the concentrations of 0.04 µM, 0.12 µM and 0.37 µM of QSN are shown. **(D)** Images from the assays performed to determine the inhibition effect of TB56 on *T. cruzi* amastigotes in infected Vero cells. Sample images from the cells treated with DMSO and 0.04 µM, 3.3 µM and 10 µM of TB56 are shown. The images shown in (B-D) are from the median 48h time point. Size bars are 100 µm for all images. **(E)** Determination of the ratio of the number of intracellular *T. cruzi* amastigotes that remain in Vero cell in cultures treated with BZN, QSN and TB56 for 24, 48 and 72 hours. For the QSN (green line) and TB56 (blue line) assays, only the concentration points with living Vero cells are shown in the graphs. As expected, the BZN (red line) treatment leads to a consistent reduction of intracellular amastigotes reaching nearly zero in the higher concentrations at the 48h and 72h time points. In the TB56 assay, the ratio of amastigotes per cell remains constant in the first 24h but decreases similarly to the BZN treatment in the 48h and 72h treatment times. In the case of QSN assay, the ratio of intracellular amastigotes increases. This indicates that the Vero cells die at a faster rate than the intracellular amastigotes. All assays were done through technical quadruplicates.

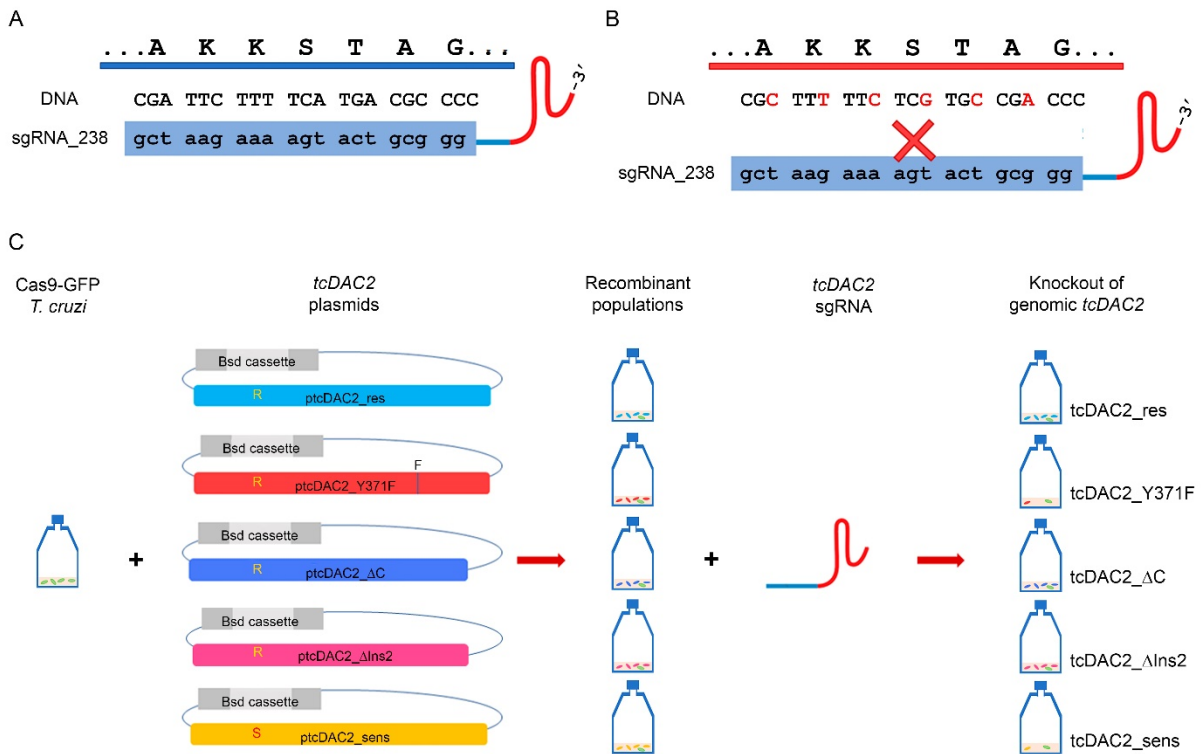


Figure S8. Cas9-cleavage resistant sequences and *tcDAC2* complementation assays. Related to Figure 2 and to STAR Methods. **(A)** Original *tcDAC2* nucleotide sequence at the sgRNA_238 recognition site. This sequence was maintained unaltered in the Cas9 sensitive variant. The sensitive variant (*tcDAC2_sens*) serves as a control for the knockout phenotype. **(B)** *tcDAC2* nucleotide sequence at the sgRNA_238 recognition site with altered nucleotides (indicated in red) to generate a Cas9-resistant variant but keeping the protein sequence unchanged. This resistant variant (*tcDAC2_res*) was combined with the catalytic site (*tcDAC2_Y371F*), C-terminal deletion (*tcDAC2_ΔC*) and loop/C-terminal deletion (*tcDAC2-ΔIns2*) mutants in *T. cruzi* expression plasmids (*tcDAC2* plasmids) allowing for gene replacement to test for complementation of genomic *tcDAC2* knockout by the plasmid-borne copy variants of *tcDAC2*. **(C)** Sequential steps of the complementation assay. Initially, *tcDAC2* plasmids were transfected into Cas9-expressing *T. cruzi* cells (left panel). After selection of the five derivative *T. cruzi* transfectants (middle panel), the recombinant populations were transfected with the *tcDAC2* sgRNA to knock out the genomic copies of *tcDAC2* (right panel) for the phenotypical analyses.

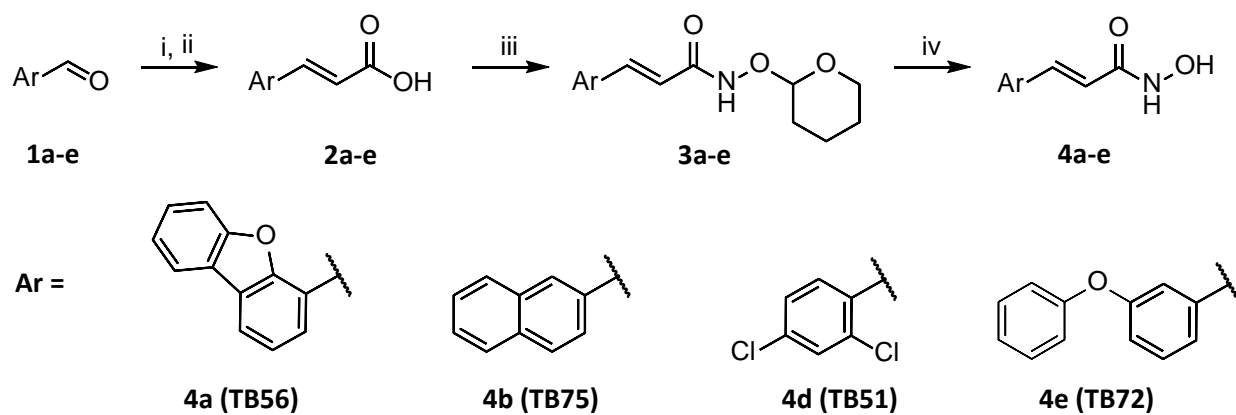


Figure S9. Scheme of synthesis of hydroxamic acids 4a-e. Related to Figure 3 and to STAR Methods.

Scheme for the synthesis of the new molecules used in this study. The different steps are summarized as follows: (i) malonic acid, pyridine, piperidine, 3-6 h, 70-80°C, (ii) HCl, 0°C, O/N, 4-8h, (iii) PyBOP, DIPEA, H₂NOTHP, THF, room temperature, O/N, and (iv) HCl, MeOH, room temperature, 6-24h.

Table S2. Data collection and refinement statistics. Related to Figures 4, 5 and 6.

Data collection*	tcDAC2/QSN	tcDAC2/TB56
Space group	I222	P2 ₁
Cell dimensions		
a, b, c (Å)	82.17, 93.58, 119.46	66.07, 95.35, 96.92
α, β, γ (°)	90.00, 90.00, 90.00	90.00, 103.50, 90.00
Resolution (Å)	50 – 1.70 (1.81 – 1.70)	50.0 – 2.3 (2.44 – 2.3)
Rsym or Rmerge	11.0 (238.7)	19.5 (168.7)
I / σI	14.2 (1.0)	7.76 (1.23)
Completeness (%)	99.9 (99.5)	99.7 (98.8)
Redundancy	13.3 (13.0)	7.00 (6.78)
CC(1/2)	99.9 (67.4)	99.5 (42.5)
Refinement		
Resolution (Å)	46.79 – 1.75	48.1 – 2.30
No. reflections	46459	51993
Rwork / Rfree	0.192 / 0.218	0.196 / 0.224
Number of atoms		
Protein	3042	6478
Ligand/ion	38	44
Water	226	230
B-factors		
Protein	39.86	45.53
Ligand/ion	39.17	66.97
Water	42.91	41.24
R.m.s. deviations		
Bond lengths (Å)	0.006	0.007
Bond angles (°)	0.743	0.927
<i>* Values in parentheses are for the highest-resolution shell.</i>		

Table S3. Sequence differences of major active site residues in Trypanosoma strains. Related to Figures 1 and 4.

Strain	E156 L2	H197 Ac Bind	H198 Ac Bind	F207 Channel	D237 Zn	H239 Zn	F267 Channel	D328 Zn	P334 L6	L335 L6	Y371 Cat
<i>T. cruzi</i>	E	H	H	F	D	H	F	D	P	L	Y
<i>T. conorhini</i>	D	H	H	F	D	H	F	D	P	L	Y
<i>T. rangeli</i>	D	N	H	F	D	H	F	D	P	L	Y
<i>T. grayi</i>	D	H	H	F	D	H	Y	D	P	I	Y
<i>T. theileri</i>	D	H	H	F	D	H	Y	D	P	L	Y
<i>T. brucei</i>	D	H	N	S	D	H	F	N	P	Y	N
<i>T. equiperdum</i>	D	H	N	S	D	H	F	N	P	Y	N
<i>T. vivax</i>	I	S	H	S	C	R	Y	D	P	D	Q

Residues diverging from canonical HDAC active site amino acids but potentially playing the same role are shown in red.

Residues potentially incompatible with a bona fide lysine deacetylase activity are shown in red and bold and are highlighted yellow.

Ac Binding: residue participating to acetyl group binding.

Channel: residue participating to the active site pocket channel accommodating the lysine side chain aliphatic part.

Zn: residue participating in zinc binding.

L2: residue of L2 loop normally interacting with the main chain of the incoming acetylated target.

L6: residue in L6 loop.